This is a preprint, the final version is subject to change, of the American Mineralogist (MSA)
Cite as Authors (Year) Title. American Mineralogist, in press.
DOI: https://doi.org/10.2138/am-2019-6623

Revision 1

In-situ iron isotope analyses reveal igneous and magmatic-hydrothermal growth of magnetite at the Los Colorados Kiruna-type iron oxide - apatite deposit, Chile.

Jaayke L. Knipping[1, 2, 3,], Adrian Fiege[1], Adam C. Simon[3], Martin Oeser[2], Martin Reich[4] Laura D. Bilenker[5]*

[1]Department of Earth and Planetary Sciences, American Museum of Natural History, Central Park West at 79th Street, New York, NY 10024-5192 (Present Address)
[2]Institut für Mineralogie, Leibniz Universität Hannover, Callinstraße 3, 30167 Hannover, Germany
[3]Department of Earth and Environmental Sciences, University of Michigan, 1100 North University Ave Ann Arbor, MI 48109-1005, USA.
[4]Department of Geology and Andean Geothermal Center of Excellence (CEGA), FCFM, Universidad de Chile, Plaza Ercilla 803, Santiago, Chile
[5]Pacific Centre for Isotopic and Geochemical Research, Department Earth, Ocean, & Atmospheric Sciences, University of British Columbia, 2020 – 2207 Main Mall, Vancouver, BC Canada V6T 1Z4

**corresponding author*

E-mail: jaaykek@umich.edu, afiege@amnh.org, m.oeser@mineralogie.uni-hannover.de, simonac@umich.edu, mreich@ing.uchile.cl , lbilenke@eoas.ubc.ca

Abstract

Iron-oxide apatite (IOA) deposits are mined for iron (Fe) and can also contain economically exploitable amounts of Cu, P, U, Ag, Co and rare earth elements (REE). Recently, it has been proposed based on trace element zonation in magnetite grains from the Los Colorados Kiruna-type IOA deposit, Chile, that ore formation is directly linked to a magmatic source. The model begins with the crystallization of magnetite microlites within an oxidized volatile-rich (H_2O+Cl) andesitic magma reservoir, followed by decompression, nucleation of fluid bubbles on magnetite microlite surfaces, segregation of a Fe-Cl-rich fluid-magnetite suspension within the magma

reservoir, and subsequent ascent of the suspension from the magma chamber via pre-existing structurally enhanced dilatant zones that act as conduits. Emplacement and precipitation of the suspension results in the formation of magnetite grains with core-to-rim features that record a transition from purely igneous to magmatic-hydrothermal conditions within IOA deposits. Here we test this model by using *in situ* femtosecond laser–ablation MC-ICP-MS measurements of Fe isotopes to determine grain-to-grain and intra-grain Fe isotope variations in magnetite grains from the Los Colorados IOA deposit. All *in situ* δ^{56}Fe values (^{56}Fe/^{54}Fe relative to IRMM-14) plot within the magmatic range (0.06 to 0.50 ‰), in agreement with previously published bulk Fe isotope analyses in magnetite from the Los Colorados IOA deposit. Different trace element signatures of these magnetite grains indicate an igneous or magmatic-hydrothermal origin, respectively. Although data partly overlap, the assigned igneous magnetites yield on average higher δ^{56}Fe values (0.24 ± 0.07 ‰; n=33), when compared to magmatic-hydrothermal magnetites (0.15 ± 0.05 ‰; n=26). Some magnetite grains exhibit a distinct core-to-rim trend from higher towards lower δ^{56}Fe signatures. Further, the δ^{56}Fe of the igneous magnetites correlate negatively with trace elements contents typical for igneous formation (Ti, Al, Ga, V, Mn, Zn); igneous magnetites become isotopically heavier with decreasing concentrations of these elements, indicating a trend towards higher δ^{56}Fe in the magnetite with magma evolution. Model calculations of the δ^{56}Fe evolution in melt, magnetite, and fluid further constrain the magmatic-hydrothermal origin of Kiruna-type IOA deposits.

Keywords: Los Colorados, Chilean Iron Belt, Kiruna-type deposits, iron oxide-apatite deposits, iron isotopes, magnetite flotation.

This is a preprint, the final version is subject to change, of the American Mineralogist (MSA)
Cite as Authors (Year) Title. American Mineralogist, in press.
DOI: https://doi.org/10.2138/am-2019-6623

Introduction

The Los Colorados iron oxide-apatite (IOA) mineral deposit is one of about fifty Kiruna-type IOA and iron oxide-copper-gold (IOCG) mineral deposits in the Chilean Iron Belt. The Chilean Iron Belt is directly linked to the crustal-scale transcurrent Atacama Fault System (Fig. 1a), which was created by the tectonic change from transtensional to transpressional stress along the South American subduction zone during the late Lower Cretaceous (Uyeda and Kanamori, 1979). The Los Colorados IOA deposit consists of two sub-parallel massive magnetite ore bodies, referred to as dikes by the mining company geologists, (Fig. 1b) and both are hosted within andesite of the Punta del Cobre Formation (Pincheira et al., 1990) along with several plutonic units (Fig. 1a). Los Colorados has proven resources of up to 986 Mt iron ore with an average grade of 34.8% (CAP-summary, 2013).

The genesis of Kiruna-type IOA deposits remains controversial, with several models proposed to explain mineralization, ranging from (non-) magmatic-hydrothermal (Menard, 1995; Rhodes and Oreskes, 1995, 1999; Barton and Johnson, 1996, 2004; Haynes et al., 1995; Rhodes et al., 1999; Haynes, 2000; Sillitoe and Burrows, 2002 and Pollard, 2006) to purely igneous processes such as liquid immiscibility between iron-rich and silicate-rich melts (e.g., Nyström and Henriquez, 1994; Travisany et al., 1995; Naslund et al., 2002; Henriquez et al., 2003; Chen et al., 2010, Hou et al. 2017, 2018). A recently proposed genetic model for Los Colorados and other Kiruna-type IOA deposits in the Chilean Iron Belt involves a synergistic combination of igneous and magmatic-hydrothermal processes to explain the complex geochemistry and textures of magnetite from the Los Colorados ore bodies (Knipping et al., 2015a, b; Rojas et al., 2018a, b).

In general, elevated concentrations of compatible and/or immobile trace elements such as Ti, V, Al, and Mn in magnetite were previously interpreted to indicate a magmatic origin (i.e.,

crystallization from a silicate melt), whereas relatively low concentrations of these elements in magnetite were interpreted to indicate a magmatic-hydrothermal origin (i.e., precipitation from a cooling aqueous fluid) (Nielsen et al., 1994; Toplis and Carrol, 1995; Dupuis and Beaudoin, 2011; Dare et al., 2012; Nadoll et al. 2014). However, at Los Colorados, some magnetite samples are characterized by trace element concentrations indicating crystallization from a melt, while other magnetite samples indicate precipitation from a hydrothermal fluid (Fig. 2). In addition, many magnetite samples from Los Colorados reveal systematic intra-grain trace element zoning of trace elements such as Ti, V, Al, Mn, with enriched magnetite cores and depleted magnetite rims, hinting at a direct transition from purely magmatic to magmatic-hydrothermal processes (Fig. 2). In order to explain this contradictory geochemistry Knipping et al. (2015a,b) proposed a magnetite flotation model, which consists of four steps: **i)** igneous magnetite crystallization from silicate melt in an andesitic magma reservoir followed by decompression-induced exsolution of volatile phase bubbles that nucleate on magnetite microlite surfaces (Fig. 3a); **ii)** further decompression-induced degassing and buoyancy-driven bubble-magnetite pair ascent (Fig. 3b); **iii)** growth and Fe enrichment of the saline bubble-magnetite suspension during continued ascent of the suspension (Fig. 3c); and **iv)** fast and efficient segregation of the magnetite suspension facilitated by hydraulic fracturing in an extensional tectonic regime (Fig. 3d). Cooling of the magnetite-fluid suspension at the final emplacement depth results in the precipitation of magmatic-hydrothermal magnetite as rims surrounding igneous magnetite grains and interstitially as matrix of the ore body (Fig. 3e). Importantly, the preferential nucleation and growth of fluid bubbles on crystal faces of oxides such as magnetite has been documented in studies of natural system, and in experiments (Hurwitz and Navon, 1994; Gardner and Denis, 2004; Gualda and Ghiorso, 2007; Edmonds et al. 2014).

In addition to systematic core-to-rim variability of trace element concentrations, the flotation model also relies on the bulk Fe isotope signature of the Los Colorados magnetite (Knipping et al., 2015a; Bilenker et al., 2016), which plots in the "magmatic range" (δ^{56}Fe = +0.06 to +0.50 ‰; Heimann et al., 2008; Weis, 2013). Thus, bulk magnetite from Los Colorados is consistent with magnetite that grew from silicate melt and/or high-temperature magmatic-hydrothermal fluid in contrast to magnetite from hydrothermal iron oxide deposits (-1.6 to ~ 0.0 ‰) (Severmann and Anbar, 2008) such as iron skarns that reveal significantly lower δ^{56}Fe values (-0.36 to + 0.01 ‰) (Weis, 2013). Despite the unambiguously magmatic/magmatic-hydrothermal Fe isotope signal recorded in magnetite from Los Colorados, the intra-grain and grain-to-grain variation in Fe isotope composition remains unconstrained. However, it is expected from the magnetite flotation model that δ^{56}Fe values would differentiate, consistent with trace-element variability, between magnetite cores (i.e. igneous magnetite enriched in, e.g., Ti, V, Al, Mn) and respective rims (i.e. magmatic-hydrothermal magnetite depleted in, e.g., Ti, V, Al, Mn) due to Fe isotope fractionation between melt-magnetite and magnetite-fluid.

The current study was motivated by recent improvements in using femtosecond laser-ablation multi-collector inductively-coupled plasma mass spectrometry (LA-MC-ICP-MS) for high-precision, high-spatial resolution Fe isotope measurements (Oeser et al., 2014). We test the Knipping *et al.* flotation model by using *in situ* LA-MC-ICP-MS Fe isotope data collected from Los Colorados magnetite grains. Notably, the measurements were performed on the same grains previously analyzed by Knipping et al. (2015a, b) for their major and trace element compositions. Our new *in situ* Fe isotope data reveal core-to-rim variations in δ^{56}Fe values that are consistent with Fe isotope fractionation processes occurring during the continuum from purely igneous to magmatic-hydrothermal conditions. We further explore the Fe isotope

variations within igneous magnetite (cores) by using model calculations of the δ^{56}Fe evolution of melt, magnetite, and fluid, providing constrains for the magmatic-hydrothermal evolution of Kiruna-type IOA systems.

Samples and analytical procedure

We analyzed 15 magnetite separate grains with *in situ* Fe isotope LA-MC-ICP-MS, wherein ten magnetite grains originate from drill core LC-04 and five from drill core LC-05 (Fig. 1b). Both drill holes crosscut the western (main) magnetite ore body of the Los Colorados deposit (Table 1). Magnetite samples from drill core LC-04 were taken at depths of 38.8, 66.7, 99.5, 104.4, 125.3 and 129.3 m from the northernmost part of the western ore body, while magnetite samples from drill core LC-05 were extracted at 20.7, 82.6, 106.0, 126.0 and 150.0 m, in the center of the western ore body. Each magnetite grain was analyzed with two to eight raster spots (~ 100 x 100μm) for a total of 69 analyses. When possible, raster spots were taken as close as possible to previous LA-ICP-MS line transects for trace element analysis measured by Knipping et al. (2015a, b); however, sample surface and inclusions sometimes inhibited measurements in the immediate vicinity.

The Fe isotope measurements were performed at the Leibniz Universität Hannover (Germany) by using a high mass resolution MC-ICP-MS (Thermo-Finnigan Neptune Plus) connected to a Spectra-Physics Solstice femtosecond laser ablation system. The laser ablation system is equipped with a 100 femtosecond Ti-sapphire regenerative amplifier, operating at a fundamental wavelength of 775 nm, which was frequency-quadrupled, resulting in a wavelength of 194 nm. The output energy was about 3.2 mJ/pulse at a fundamental wavelength of 775 nm. Pumping with 500 Hz resulted in a pulse energy of 70 μJ at a wavelength of 194 nm. We used the ablation

cell and stage/visualization system (modified New Wave LUV 266) as described in Horn et al. (2006) and Horn and von Blanckenburg (2007). The femtosecond LA-MC-ICP-MS Fe isotope measurements were performed at high mass resolution ($M/\Delta M \approx 9000$, 5–95% peak side width definition) to resolve molecular interferences of argon nitrides and argon oxides on Fe isotopes (and also potentially sample-induced interferences of CaO and CaN; see Weyer and Schwieters 2003). Employment of an H-type skimmer cone for the *in situ* Fe isotope determinations resulted in normal intensities of interfering argon oxides and argon nitrides, i.e., < 1V. All analyses were performed by using a raster technique in which areas of ~ 100 µm x 100 µm were ablated by using a 50-60 µm spot size.

The Fe isotope compositions are reported using delta notation, and $\delta^{56}Fe$ values are given as variation in parts per million (‰) from the composition of IRMM-14 (Institute of Reference Materials and Measurements standard 014).

$$\delta^{56}Fe = [((^{56}Fe/^{54}Fe)_{sample}/(^{56}Fe/^{54}Fe)_{IRMM\text{-}14})\text{-}1]\times 1000 \qquad \text{equation 1}$$

The IRMM-14 standard was measured after every 1-2 sample analyses for drift monitoring. Horn et al. (2006) demonstrated that this procedure yields absolute values with a high accuracy of ≤ 0.1 ‰ for $\delta^{56}Fe$ in oxides, hydroxides, carbonates metals and sulfides (see their Fig. 9). The high accuracy was confirmed by session-to-session and in-session monitoring of an internal secondary pure Fe reference material ("puratronic", Johnson Matthey, lot No. FE495007IF2, 99.995% Fe) for which we reproduced the absolute $\delta^{56}Fe$ within ± 0.05 ‰. Importantly, during our *in situ* Fe isotope analyses a Ni reference solution (NIST SRM 986, 5 ppm Ni in 0.5 M HNO_3 solution) was added via a quartz glass spray chamber and introduced into the plasma along with the

ablation aerosol in order to (a) use the measured Ni isotope ratios as an external mass bias monitor (Oeser et al., 2014), and (b) maintain "wet" plasma conditions. As demonstrated by Zheng et al. (2018), potential matrix effects during *in situ* Fe isotope analyses by fs-LA-MC-ICP-MS are drastically reduced under such "wet" plasma conditions, enabling us to perform accurate and precise Fe isotope measurements without matrix-matching of sample (magnetite) and standard (metal).

Each analytical spot analysis was measured for ^{54}Fe, ^{56}Fe and ^{57}Fe, and the calculated ratios of $^{56}Fe/^{54}Fe$ and $^{57}Fe/^{54}Fe$ and the resulting $\delta^{56}Fe$ and $\delta^{57}Fe$ values are plotted against each other in Fig. 4, revealing a slope of 1.42 (R^2=0.9) , which is in good agreement with the mass dependent fractionation ratio of 1.47 that is based on the natural abundances of Fe isotopes; ^{54}Fe = 5.85% ; ^{56}Fe = 91.75; ^{57}Fe = 2.12% (e.g., Dauphas and Rouxel, 2006), as we do not expect any mass-independent fractionation during measurements (Horn et al., 2006). Thus, fractionation factors from the literature given in $\delta^{57}Fe$-notation can be simply recalculated into $\delta^{56}Fe$-notation, or vice versa, when comparing them with our data. Further details about the method are provided in Horn et al. (2006) and Oeser et al. (2014).

Results

The *in situ* $\delta^{56}Fe$ values for magnetite from Los Colorados range from 0.04 to 0.38 ‰ (n=69; Table 1), wherein samples from drill core LC-05 have a more narrow range (0.06 to 0.27 ‰) when compared to samples from drill core LC-04. Some magnetite grains are zoned from heavier $\delta^{56}Fe$ values in magnetite cores to lower values in magnetite rims (e.g., sample LC-05-82.6: 0.24 ± 0.02 ‰ in the core versus 0.16 ± 0.04 ‰ in the rim). Other samples show constant low $\delta^{56}Fe$ values (e.g., sample LC-05-126: 0.11 ± 0.02‰), or constant high $\delta^{56}Fe$ values (e.g., sample LC-

196 04-38.8d: 0.33 ± 0.06‰) without obvious zoning (Table 1). One exception is sample LC-05-
197 20.7, which shows zoning from lighter δ^{56}Fe values in the core (0.07 ± 0.01‰) towards
198 relatively heavier δ^{56}Fe values in its rim (0.13 ± 0.02‰). In order to interpret these Fe isotope
199 signatures, we will use the textural appearance and sample depths information of magnetite
200 grains combined with trace element data published by Knipping et al. (2015b) to assign the
201 results of this study to magmatic-hydrothermal and igneous origin.
202

203 **Discussion**

204 ***Igneous vs. magmatic-hydrothermal magnetite***

205 Almost all of the δ^{56}Fe values measured in this study plot in the magmatic range (0.06-0.50 ‰)
206 (Table 1) defined by Heimann et al. (2008), and are consistent with previous bulk δ^{56}Fe data of
207 entire magnetite grains from the same samples analyzed by traditional solution MC-ICP-MS
208 (Knipping et al., 2015a; Bilenker et al., 2016). In these samples, Knipping et al. (2015a,b)
209 discovered systematic variation in trace element abundances of, e.g., Ti, Al, Mn, between
210 magnetite cores and rims, interpreted by those authors as evidence for the crystallization of
211 magnetite cores from a silicate melt (i.e., igneous magnetite) followed by the precipitation of
212 magnetite rims and matrix magnetite (i.e., interstitial magnetite) from a fluid phase derived from
213 the same magma reservoir (i.e., magmatic-hydrothermal magnetite). In order to determine
214 whether the new Fe isotope data indicate an igneous and/or magmatic-hydrothermal origin for
215 magnetite, trace element transects collected using LA-ICP-MS by Knipping et al. (2015b) and
216 sample depths information were used to initially distinguish (see supplementary material).
217 Magnetite has an inverse spinel structure in which ferrous Fe can be substituted by divalent (Mg,
218 Ni, Mn, Co and Zn) and ferric Fe by trivalent cations (Al, Cr, V, Mn and Ga) as well as by Ti^{4+}

in combination with a divalent cation (Lindsley, 1976; Wechsler et al. 1984; Ghiorso and Evans, 2008). A higher concentration of these compatible elements, especially elements that are immobile in fluids, e.g., Ti and Al (Van Baalen, 1993; Verlaguet et al. 2006), are robust indicators of an igneous formation. According to many studies, Ti and Al are the best trace elements to discriminate between igneous and hydrothermal magnetite because they are mainly detected in high temperature igneous magnetite (Nielsen et al., 1994; Toplis and Carrol, 1995; Dupuis and Beaudoin, 2011; Dare et al., 2012; Nadoll et al. 2014).

Thus, we used Ti and Al concentrations in Los Colorados magnetite as a proxy for discrimination between igneous (core) and hydrothermal (rim) magnetite. Fig. 5 shows an example of a previous LA-ICP-MS trace element transect (Knipping et al. 2015b) in proximity to the *in situ* Fe isotope measurements. A sudden decrease in Ti and Al concentration was detected when measuring from core to rim. Hence, the raster spot A (δ^{56}Fe = 0.16 ± 0.04 ‰) is assigned as magmatic-hydrothermal magnetite "rim", whereas the remaining raster spots B-F (δ^{56}Fe = 0.19-0.24 ± 0.05 ‰) are interpreted as igneous magnetite "core". Also other measured grains show this kind of zoning where isotopically heavier Fe is concentrated with a high concentration of compatible and/or immobile elements (e.g., Ti and Al) in the center of the grains, and isotopically lighter Fe and lower concentrations of these elements exist in the rims of the grains (Table 1). In contrast, samples LC-04-66.7b, LC-04-129.3c, and LC-05-126 have constantly low concentrations of Ti (~ 110, ~ 3800 and ~ 650 ppm) and Al (400-700, ~1800 and ~ 1900 ppm), and were assigned as magnetite formed solely under magmatic-hydrothermal conditions, whereas samples LC-04-129.3d and LC-05-150b show constantly higher concentrations of trace elements typical for an igneous origin (Ti = 4800-5400 and ~7400 ppm; Al = 5000-5500 ppm and ~ 5100 ppm) (see supplementary material). The samples analyzed from Los Colorados were

fragments of massive magnetite that sometimes show distinct magnetite cores with magmatic-hydrothermal rims or within a massive magmatic-hydrothermal magnetite matrix (Fig. 3e, area A). However, some areas may reflect completely magmatic-hydrothermal matrix magnetite, which precipitated in void spaces after cooling (Fig. 3e, area B), while other locations likely reveal aggregates of several accumulated igneous magnetite crystals (Fig. 3e, area C).

Simultaneously, the magnetite samples without trace element zoning, i.e., with constant low or constant high trace element concentration (e.g., Ti and Al), also have relatively constant Fe isotope ratios without any obvious zoning (LC-04-66.7b: 0.15 - 0.22 ‰, LC-04-129.3c: 0.04 - 0.11 ‰, LC-05-126: 0.09 - 0.13 ‰, LC-04-129.3d: 0.18 - 0.24 ‰, LC-05-150b: 0.14 – 0.20 ‰). The anomalous sample LC-05-20.7, which yielded lighter Fe isotope values in its core (0.07 ± 0.05 ‰) versus relatively heavier Fe isotope values in its rim (0.14 ± 0.06 ‰), contains high Ti (2400-2600 ppm) and Al concentrations (4400-4800 ppm) throughout the grain indicating an exclusively igneous formation.

After assigning all *in situ* Fe isotope values to their probable origin (i.e., igneous vs. magmatic-hydrothermal, Table 1 and supplementary material) based on textural and trace element chemical data and plotted versus sample depth for each drill core, a systematic pattern is revealed (Fig. 6), where δ^{56}Fe decreases from relatively heavy values (δ^{56}Fe= 0.24 ± 0.07 ‰; 2SD with n=33) in primary igneous magnetite to relatively lower values (δ^{56}Fe= 0.15 ± 0.05 ‰; 2SD with n=26) in magmatic-hydrothermal magnetite. However, there is an additional trend within the purely igneous realm (i.e., red data in Fig. 7) indicating increasing δ^{56}Fe with decreasing compatible and/or immobile trace elements (e.g., Ti, Al, V, Ga, Zn and Mn) in magnetite, which provide new insights on the transition between the igneous phase of magnetite crystallization to the subsequent magmatic-hydrothermal stage.

265

266 ***Igneous magnetite crystallization***

267 Observations from empirical and experimental studies indicate that elements such as Al, Mn, Ti,
268 V, Ga and Zn are typically enriched in magmatic magnetite, and that the concentrations of trace
269 elements in magnetite increase systematically with increasing temperature (Nadoll et al., 2014;
270 Toplis and Carroll, 1995). This is in agreement with the observed enrichment of Ti and Al in
271 magnetite from more primitive silicate melts when compared to more evolved systems (Dare et
272 al., 2012; Grigsby, 1990; Lindsley, 1991). Thus, higher concentrations of Al, Mn, Ti, V, Ga and
273 Zn are expected in magnetite that nucleates and grows during early magmatic stages, while
274 relatively lower concentrations of trace elements in igneous magnetite may indicate growth
275 during a later magmatic stage (indicated by red arrow in Fig. 7). Hence, the magnetite sample
276 with highest concentration of Al, Mn, Ti, V, Ga and Zn (LC-05-150) is interpreted here as the
277 most primitive magnetite composition, which simultaneously reveals among the lowest $\delta^{56}Fe_{mgt}$
278 values (0.14 to 0.20 ‰) of igneous magnetite (red data in Fig. 6) measured at Los Colorados. A
279 potential parental melt can be calculated for these $\delta^{56}Fe_{mgt}$ data by using equation 2, which was
280 determined by Sossi et al. (2012) based on tholeiitic samples of the Red Hill intrusion.

281

282 $\Delta^{56}Fe_{mgt\text{-}melt} = \delta^{56}Fe_{mgt} - \delta^{56}Fe_{melt} = \Delta^{56}Fe_{mgt\text{-}melt} * 1.47 = +0.20$ ‰ $* 10^6/T^2$; T in K equation 2

283

284 The derived $\delta^{56}Fe_{melt}$ values (0.07 to 0.13 ‰ at 1125 °C; i.e., the temperature of first crystallizing
285 magnetite) are in agreement with the average bulk Fe isotope composition ($\delta^{56}Fe_{bulk} = 0.11 \pm$
286 0.05‰) of silicate rocks ranging between 55-70 wt% SiO_2 determined by various studies (Table
287 2; e.g., Poitrasson and Freydier, 2005; Schoenberg and von Blanckenburg, 2006; Heimann et al.

2008; Teng et al. 2008; Schüssler et al., 2009; Sossi et al., 2012; Telus et al., 2012; Zambardi et al., 2014), which is in agreement with the local and regional geology around Los Colorados (andesitic host rock and dioritic plutons) (Fig. 1).

However, the igneous magnetite at Los Colorados with lower concentrations of Ti, V, Al, Mn, Ga and Zn (Fig. 7) reveal a heavier Fe isotope composition ($\delta^{56}Fe_{mgt}$ up to 0.38 ‰), consistent with magnetite that would have need to be crystallized from a melt with a significantly higher $\delta^{56}Fe_{melt}$ (up to 0.30 ‰ at T = 1050 °C). Such heavy Fe isotope compositions are often measured in silicate rocks with more evolved compositions (SiO_2 > 70 wt%) when compared to andesite.

Initially, this observation was explained by the exsolution of deuteric fluids during late differentiation stages (Poitrasson and Freydier, 2005; Heimann et al. 2008; Telus et al., 2012). Exsolved magmatic-hydrothermal fluids were supposed to preferentially leach ferrous Fe and, thus, relatively light $\delta^{56}Fe$ from the silicate melt (Poitrasson and Freydier, 2005; Heimann et al. 2008; Telus et al., 2012; Bilenker et al., 2012); e.g., $\delta^{56}Fe_{fluid}$ = -0.05 to -0.39 ‰ at 500 and 700 °C (Heimann et al., 2008).

Although the fractionation effect by deuteric fluids at late differentiation stages was recently determined to be of minor importance in order to explain the increasing $\delta^{56}Fe_{bulk}$ of rocks with SiO_2 >70 wt% (Dauphas et al. 2017), it may still play a significant role for early fractionation melt-dominant magmas that exsolve fluids during degassing processes caused by magma ascent or overlaying pluton formation.

Thus, a degassing melt would become enriched in heavy $\delta^{56}Fe$ resulting in crystallizing igneous magnetite that would consequently incorporate also increasingly heavier Fe isotopes as a function of degassing ($\delta^{56}Fe_{mgt}$ > 0.18 ‰.), correlating negatively with trace element concentrations in magnetite, such as Ti, V, Ga, Mn, Zn and Al (Fig. 7). This is because Ti, V,

311 Ga, Mn, and Zn are compatible in magnetite relative to silicate melts (Nielsen, 1992; Okamoto,
312 1979; La Tourette et al., 1991; Ewart and Griffin, 1994) and ongoing decompression-induced
313 crystallization of magnetite itself would lower their concentrations in the residual melt. In
314 addition, decompression-induced degassing of a (sulfur-poor) system may increase oxygen
315 fugacity of the system (Mathez, 1984; Burgisser and Scaillet, 2007; Bell and Simon, 2011) and,
316 thus, may affect the oxidation state of V and Mn, limiting the substitution into magnetite's
317 structure. In contrast the partitioning of Sn into magnetite may increase with increasing oxygen
318 fugacity (Carew, 2004) which is consistent with correlating higher Sn values and heavier Fe
319 isotope signatures that are caused during degassing of the melt (Fig. 8). Manganese and Zn are
320 compatible in magmatic-hydrothermal fluid (Zajacz et al., 2008) and degassing would therefore
321 decrease the concentration of these elements in magnetite even more significantly. In contrast, Al
322 is a major element in silicate melts and incompatible in magnetite ($D^{mgt/melt}_{Al}$=0.117; La Tourette
323 et al., 1991), and is often considered as an immobile element in magmatic-hydrothermal fluid
324 (e.g., Carmichael, 1969). However, this characterization is mainly based on the low solubility of
325 aluminum hydroxides and aluminum silicates in aqueous fluids. Indeed, more recent
326 experimental studies (e.g., Verlaguet et al., 2006) have shown that Al can be mobile despite its
327 low solubility in aqueous fluid. This mobility is especially pronounced during disequilibrium
328 processes such as fluctuations in pressure, temperature, and fluid composition. Thus, a kinetic
329 degassing process may be capable of leaching Al from the melt into the fluid phase, resulting in a
330 decreasing Al content in magnetite with continued degassing, while $\delta^{56}Fe_{mgt}$ increases (Fig. 7).
331
332 ***Magmatic-hydrothermal magnetite precipitation***

The extensional tectonic stress in the Atacama Fault System promotes ongoing decompression and allows an efficient separation of the fluid-magnetite suspension from the parental magma reservoir and its rapid transport via hydraulic fractures in crustal fault systems. The dissolved $FeCl_2$ in the fluid-magnetite suspension will precipitate magmatic-hydrothermal magnetite due to the decreasing solubility of $FeCl_2$ at hydrothermal temperatures (~ 450-620 °C) that is more effective with the degree of decompression, i.e. rapid decompression may lead to the formation of larger ore bodies (Simon et al., 2004; Rojas et al. 2018). The magmatic-hydrothermal magnetite will precipitate as rims and as matrix surrounding the igneous magnetite grains or accumulation of igneous grains (Fig. 3e) (Knipping et al., 2015a,b). Accordingly, the hydrothermally precipitated magnetite contains relatively high concentrations of compatible and mobile elements like Mn and Zn that are almost as high as in the igneous magnetite (Fig. 7), when compared to immobile elements that are more depleted in the hydrothermally precipitated magnetite. However, a clear trend towards isotopically heavy or light Fe isotope composition with trace element variation, as observed for the igneous magnetite domains, is not detectable for the magmatic-hydrothermal magnetite (Fig. 7 and 8). The constant value of $\delta^{56}Fe = 0.15 \pm 0.05$ ‰ for the magmatic-hydrothermal magnetite probably indicates one fast depositional event at a certain pressure and temperature (Rojas et al. 2018). When applying equation 3 (Heimann et al., 2008) for the calculation of magnetite-fluid Fe isotope fractionation, the Fe isotope composition of a hypothetical parental magmatic-hydrothermal fluid ranges from -0.15 to -0.32 ‰ for temperatures between 700 and 500 °C; this range is consistent with Fe isotope compositions of magmatic-hydrothermal fluids ($\delta^{56}Fe_{fluid}$ = -0.05 to -0.39 ‰) estimated by Heimann et al. (2008).

$$\Delta^{56}Fe_{mgt\text{-}fluid} = \delta^{56}Fe_{mgt} - \delta^{56}Fe_{fluid} = +0.28 \text{ ‰} * 10^6/T^2; \text{ T in K} \quad \text{equation 3}$$

Equation 3 predicts a $\Delta^{56}Fe_{mgt\text{-}fluid}$ value of +0.25 ‰ at 800 °C, which, we highlight, is fairly consistent with the results of recent magnetite-fluid Fe isotope fractionation experiments in the presence of a 2 M $FeCl_2 \cdot 4H_2O$ solution that yielded fractionation factors of $\Delta^{56}Fe_{mgt\text{-}fluid}$ of +0.35 ‰ (based on measured $^{56}Fe/^{54}Fe$ in experimental fluids) or +0.30 ‰ (re-calculated from $\Delta^{57}Fe_{mgt\text{-}fluid}$) at 800 °C (Sossi and O'Neill, 2017).

Iron isotope fractionation model

To explain the observed variation in Fe isotope composition among magnetite grains, we developed an holistic Fe isotope fractionation model for the formation of the Los Colorados magnetite. These calculations take into account the *magnetite-flotation model* for Kiruna-type IOA deposits developed by Knipping et al. (2015a,b) and serves as a first order verification of this model.

During the four steps of the magnetite-flotation model, three stages of Fe fractionation can be distinguished: crystallization of magnetite from the melt in a parent magma chamber (i.e., $\delta^{56}Fe$ fractionation between magnetite-melt; **Stage 1**), decompression-induced crystallization of igneous magnetite from a degassing melt during magma ascent (i.e., $\delta^{56}Fe$ fractionation between melt-fluid and magnetite-melt; **Stage 2**), and precipitation of magnetite from a segregated magmatic-hydrothermal fluid (i.e., $\delta^{56}Fe$ fractionation between magnetite-fluid; **Stage 3**). Here, the current ("snapshot") Fe isotope compositions of magnetite grown during Stage 2-3 are predicted to estimate the maximum variability in $\delta^{56}Fe_{mgt}$ in the system presuming negligible re-equilibration after crystallization/precipitation during fast open system degassing. This procedure allows us to compare the modeled range of $\delta^{56}Fe$ to the measured *in situ* range.

377

378 ***Stage 1: Initial magnetite crystallization***

379 Stage 1 of the model simulates cooling of a magma reservoir after emplacement from $T_{liquidus}$ to a
380 reasonable pre-eruptive storage T of 1050 °C, resulting in initial crystallization of magnetite
381 from silicate melt (*initial igneous mgt*) (Fig. 9a).

382 The Los Colorados Kiruna-type IOA deposit is located within the andesitic Punta del Cobre
383 formation, which is a formation typical for arc settings and, thus, andesite (i.e., P1D andesite
384 from Martel et al., 1999) is used as the source magma composition for the following predictions.
385 Arc magmas are typically hydrous (2-8 wt% H_2O) and oxidized (NNO+0 to NNO+4; in log units
386 oxygen fugacity (fO_2) relative to the Ni-NiO oxygen buffer) (Carmichael, 1991), while crustal
387 thinning in back-arc settings allows for the storage of relatively hot magma (> 1000 °C) at
388 intermediate depths (3-10 km ~ 100-400 MPa). We used the software package MELTS (cf.
389 Ghiorso and Sack, 1995) to predict cooling- and decompression-induced magma evolution; i.e.,
390 magnetite, melt, and fluid fractions, and residual melt composition (see Fig. 9). We assume an
391 initial bulk water content of 6 wt%, an fO_2 of NNO+3, and an initial pressure of 250 MPa (depth
392 ~7 km). For these parameters, MELTS predicts magnetite as the liquidus phase with a liquidus
393 temperature ($T_{liquidus}$) of 1125 °C, in agreement with experiments by Martel et al. (1999), where
394 magnetite was the liquidus phase in andesite at T > 1040 °C, 200 MPa and NNO+2 to NNO+3.

395 The bulk Fe isotope composition of the andesitic magma reservoir was set at $\delta^{56}Fe_{melt}$ = 0.11 ‰
396 (see Section 4.2; red star in Fig. 10). When applying equation 2 for the calculation of Fe isotope
397 fractionation between magnetite-melt, the first magnetite grains to crystallize from the andesitic
398 melt have a $\delta^{56}Fe_{mgt}$ of 0.18 ‰. Cooling of the andesitic magma reservoir results in continued
399 crystallization of magnetite, which preferentially incorporates heavy Fe isotopes due to its

elevated ferric/ferrous Fe composition (Bigeleisen and Mayer, 1947; Polyakov et al., 2007; Schauble, 2004; Schauble et al., 2009). Thus, the $\delta^{56}Fe$ of the model parental melt ($\delta^{56}Fe_{melt}$) decreases during magnetite crystallization and equilibration as long as only magnetite is crystallizing. Here, magnetite-melt Fe isotope equilibrium fractionation is likely, considering that cooling rates in magma reservoirs are typically low (often <200 °C/Ma; e.g., Hess et al., 1993). For instance, the crystallization of a total of 2.43 wt% magnetite (calculated with MELTS for 1050 °C) (Fig. 9a) would decrease the $\delta^{56}Fe_{melt}$ from 0.11 ‰ (bulk) to 0.08 ‰, calculated by using equation 4 (Fig. 10; Stage 1)

$$\delta^{56}Fe_{melt} = \delta^{56}Fe_{bulk} - f * \Delta^{56}Fe_{mgt\text{-}melt} \quad \text{equation 4}$$

where $\delta^{56}Fe_{bulk}$ is the bulk Fe isotopic composition of the system, f is the Fe fraction used from melt (here by only magnetite crystallization) and $\Delta^{56}Fe_{mgt\text{-}melt}$ is the temperature dependent fractionation factor between magnetite and melt (equation 2). The coexisting magmatic magnetite (i.e., *initial igneous mgt*) has a predicted $\delta^{56}Fe_{mgt}$ of 0.16 ‰ (grey star in Fig. 10), presuming equilibrium fractionation at 1050 °C, which is 0.02 ‰ lighter than the first crystallizing magnetite grains (black star in Fig. 10).

Stage 2: Igneous magnetite crystallization during magma decompression

Stage 2 represents magma ascent from intermediate depths (~7 km) to shallow depths (~2 km), resulting in decompression-induced volatile saturation of the silicate melt and leading to additional igneous magnetite crystallization in the presence of a fluid phase owing to an increase of $T_{liquidus}$.

Decompression of the volatile-rich magma, e.g., through overlaying pluton formation common in this region (Fig. 1) or magma ascent, would lead to the exsolution of volatiles and crystallization of *new igneous mgt* (Fig. 9a). In order to estimate the Fe isotope fractionation between all three phases (i.e., melt-fluid, magnetite-melt), the Fe fraction among these phases must be quantified. The Fe concentration in the fluid is dependent on the Cl concentration of the fluid (Simon et al. 2004). Here, a Cl concentration of 35 wt% $NaCl_{eq}$ is estimated for the exsolved fluid (molality, m=5.9 mol/kg) based on observations of euhedral halite crystals in magnetite hosted fluid inclusions (Knipping et al. 2015b). This allows the application of a partition coefficient of $D^{f/m}_{Fe}$=8.5 between fluid and melt according to the experimentally derived relationship: $D^{f/m}_{Fe}$=1.44*m (Zajacz et al., 2008). Thus, the exsolved fluid at a low P of 75 MPa accounts for 14 % of the total Fe, while the *initial igneous mgt* scavenges 41 % Fe and the *new igneous mgt* (magnetite crystallized between 250 and 75 MPa at 1050 °C) scavenges only 9 % Fe, leaving 35% Fe for the remaining melt (Fig. 9b). There are no published experimentally determined Fe isotope fractionation factors for melts and aqueous fluids. Thus, we estimate a fractionation factor based on an assumed initial light Fe isotope composition for the exsolving magmatic fluid of $\delta^{56}Fe_{fluid}$ = -0.39 ‰ (c.f., Heimann et al., 2008) at the beginning of the degassing (filled blue star in Fig. 10). This implies that $\Delta^{56}Fe_{melt\text{-}fluid}$ = 0.47 at 1050 °C (equation 5), when using the final value of $\delta^{56}Fe_{melt}$ of Stage 1.

$$\Delta^{56}Fe_{melt\text{-}fluid} = \delta^{56}Fe_{melt} - \delta^{56}Fe_{fluid} \qquad \text{equation 5}$$

In this model scenario, the exsolution of fluid would have a stronger effect on Fe isotope fractionation than decompression-induced magnetite crystallization. Thus, when assuming closed

system equilibrium fractionation, the continuous exsolution of a saline fluid phase would increase $\delta^{56}Fe_{fluid}$ from -0.39 ‰ at 250 MPa to -0.33 ‰ at 75 MPa (equation 6) and consequently, $\delta^{56}Fe_{melt}$ would increase from 0.08 to 0.13 ‰ (equation 7), resulting in all magnetite being as heavy as 0.22 ‰ at 75 MPa (equation 8).

$$\delta^{56}Fe_{fluid} = x\Delta^{56}Fe_{mgt\text{-}melt} + x\Delta^{56}Fe_{melt\text{-}fluid} - \delta^{56}Fe_{bulk} + y\Delta^{56}Fe_{melt\text{-}fluid} \quad \text{equation 6}$$

$$\delta^{56}Fe_{melt} = \delta^{56}Fe_{fluid} + \Delta^{56}Fe_{melt\text{-}fluid} \quad \text{equation 7}$$

$$\delta^{56}Fe_{mgt} = (\delta^{56}Fe_{bulk} - y\delta^{56}Fe_{melt} - z\delta^{56}Fe_{fluid}) / x \quad \text{equation 8}$$

In equation 8, x is the Fe fraction used by all igneous magnetite (*initial igneous mgt* + *new igneous mgt*), y is the Fe fraction used by the melt, and z is the Fe fraction used by the fluid, i.e., $x + z = 1 - y = f$, which is the Fe fraction used from melt.

An open system Rayleigh style fractionation would further increase $\delta^{56}Fe_{melt}$, from 0.08 to 0.21 ‰ (equation 9) and $\delta^{56}Fe_{fluid}$ from -0.39 to -0.26 ‰ (equation 10), resulting in a maximum $\delta^{56}Fe_{mgt}$ of 0.29 ‰ (equation 2) (Fig. 10 - Stage 2).

$$\delta^{56}Fe_{melt} = ((1000 + \delta^{56}Fe_{initial\text{-}M2}) * f^{(1-\alpha)}) - 1000 \quad \text{equation 9}$$

$$\delta^{56}Fe_{fluid} = (1000 + \delta^{56}Fe_{melt}) / \alpha - 1000 \quad \text{equation 10}$$

In equation 9, *f* equals the sum of *new igneous mgt* (magnetite growing during degassing) and fluid fraction (x_{new}+z), $\delta^{56}Fe_{initial\text{-}M2}$ is the Fe isotopy of the melt at the beginning of *Stage 2* ($\delta^{56}Fe_{initial\text{-}M2} = 0.08$ ‰) and $\Delta^{56}Fe^{melt\text{-}fluid} \approx 1000 \ln(\alpha)$.

Considering that both fractionation styles are end member scenarios, we also calculated an intermediate scenario in which magnetite (*new igneous mgt*) and aqueous fluid are extracted only once from the system during degassing at an intermediate pressure step of 150 MPa; this is referred to as "open system - one step" fractionation in Fig. 10. This scenario would increase $\delta^{56}Fe_{fluid}$ from -0.39 to -0.28 ‰ (equation 11), $\delta^{56}Fe_{melt}$ from 0.08 to 0.19 ‰ (equation 12) and result in a maximum $\delta^{56}Fe_{mgt}$ value as heavy as 0.27 ‰ (equation 13).

$$\delta^{56}Fe_{fluid} = x\Delta^{56}Fe_{mgt\text{-}melt} + x\Delta^{56}Fe_{melt\text{-}fluid} - \delta^{56}Fe_{one\text{-}step} + y\Delta^{56}Fe_{melt\text{-}fluid} \quad \text{equation 11}$$

$$\delta^{56}Fe_{melt} = \delta^{56}Fe_{fluid} + \Delta^{56}Fe_{melt\text{-}fluid} \quad \text{equation 12}$$

$$\delta^{56}Fe_{mgt} = (\delta^{56}Fe_{one\text{-}step} - y\delta^{56}Fe_{melt} - z\delta^{56}Fe_{fluid}) / x \quad \text{equation 13}$$

Here, $\delta^{56}Fe_{one\text{-}step}$ is the Fe isotopic composition of the melt calculated for the desired step (e.g., 150 MPa) using equations 6 and 7, but excluding the *initial mgt* from the Fe fractions between melt, aqueous fluid and *new igneous mgt*.

Consequently, degassing of a saline fluid with an initial $\delta^{56}Fe_{fluid}$ as light as -0.39 ‰ (Heimann et al., 2008) would increase $\delta^{56}Fe_{mgt}$ of the *new igneous mgt* (i.e., magnetite that crystallizes during decompression) to be as isotopically heavy as the measured natural igneous magnetite samples from Los Colorados (Table 1), shown as a red field in Fig. 10. Importantly, this is consistent with the measured increasing $\delta^{56}Fe_{mgt}$ values in igneous magnetite with decreasing concentrations of trace elements such as Ti, Al, Mn, V, Ga and Zn (Fig. 7).

Stage 3: Magmatic-hydrothermal magnetite precipitation during fluid cooling

Stage 3 of the model simulates magnetite precipitation from an aqueous fluid as a result of cooling. This fluid was separated from the source magma at the end of Stage 2, together with significant amounts of igneous magnetite (i.e., a fluid-magnetite suspension).

The evolution of $\delta^{56}Fe_{mgt}$ for magnetite that precipitates from the magmatic-hydrothermal fluid can be predicted as a function of decreasing temperature (e.g., from 800 to 400 °C) by using equation 3. As a first order assumption, we suggest that the Fe isotope composition of this magmatic-hydrothermal magnetite is best approximated by (open system) Rayleigh crystallization (equation 14).

$$\delta^{56}Fe_{fluid}^{f} = (1000 + \delta^{56}Fe_{initial\text{-}F3}) * f^{(\alpha-1)}) - 1000 \quad \text{equation 14}$$

The "snapshot" $\delta^{56}Fe_{mgt}^{f}$ at a given fraction *f* can then be determined by equation 15:

$$\delta^{56}Fe_{mgt}^{f} = \Delta^{56}Fe_{mgt\text{-}fluid} + \delta^{56}Fe_{fluid}^{f} \quad \text{equation 15}$$

where $\Delta^{56}Fe_{mgt\text{-}fluid} \approx 1000 \ln(\alpha)$. We assume an initial Fe isotope composition of the fluid of $\delta^{56}Fe_{initial\text{-}F3}$ = -0.26 ‰, which is the heaviest predicted δ^{56}Fe value at the end of *Stage 2* (white star in Fig. 10). Thus, the predicted Fe isotope composition of the magmatic-hydrothermal magnetite represents the maximum possible value (i.e., isotopically heaviest).

Model calculations for *Stage 3* indicate that the measured $\delta^{56}Fe_{mgt}$ value of the magmatic-hydrothermal magnetite, shown as a blue field in the Fig. 10, is reproduced by the proposed model scenario (i.e., Rayleigh fractionation), if precipitation occurs during cooling from 600 to

400 °C. However, the slightly elevated $\Delta^{56}Fe_{mgt\text{-}fluid}$ values determined experimentally by Sossi and O'Neill (2017) at 800 °C, when compared to the model values predicted by equation 3, indicate that precipitation temperatures may have exceeded 600 °C. These temperatures are consistent with fluid inclusion studies of IOA/IOCG deposits in Chile and Peru, where homogenization temperatures range from 150 to 550 °C, with some >800 °C (Bromann et al, 1999; Chen 2010; Kreiner 2011; Velasco and Tornos 2009; Barton, 2014). Notably, the estimated pressures (50-150 MPa) and fluid salinities (6-50 wt% $NaCl_{eq}$) in these studies are consistent with the predicted conditions of our model (i.e., P_{final}< 75 MPa, magmatic-hydrothermal fluid composition of 35 wt% $NaCl_{eq}$). The remaining iron in the hydrothermal fluid (>60 %) can further ascend and eventually precipitate at lower temperatures and pressures forming potentially IOCG deposits stratigraphically above IOA deposits (Knipping et al. 2015 a and b).

Implications

New *in situ* Fe isotope data, used in conjunction with trace element compositions (e.g., Ti, Al), textural observations and sample depth information, can help to distinguish igneous magnetite cores from magmatic-hydrothermal magnetite rims in the Los Colorados Kiruna-type IOA deposit, Chile. The model presented explains the measured $\delta^{56}Fe$ variability within magnetite grains, where hydrothermal parts are lighter than igneous parts. When trace elemental compositions and sample depths information are taken into account for those magnetite grains that show no zoning in order to discriminate between igneous and hydrothermal magnetite, most of the interpreted purely magmatic-hydrothermal magnetites have on average lower $\delta^{56}Fe$ when compared to purely igneous magnetites. The sum of all results reveal a systematic pattern at Los

Colorados where $\delta^{56}Fe$ is on average higher in igneous magnetite (mean $\delta^{56}Fe$= 0.24 ± 0.07 ‰; n=33) when compared to magmatic-hydrothermal magnetite (mean $\delta^{56}Fe$= 0.15 ± 0.05 ‰; n=26).

Using magnetite-melt, melt-fluid, and magnetite-fluid Fe isotope fractionation factors, we predict the evolution of $\delta^{56}Fe_{mgt}$ in purely igneous magnetite formed during crystallization from a cooling (Stage 1) and decompression-induced degassing silicate melt (Stage 2), and precipitation of magmatic-hydrothermal magnetite from a cooling exsolved saline magmatic-hydrothermal fluid (Stage 3). These stages, and their pressure-temperature evolution, are modeled in accordance with the *magnetite-flotation model* proposed by Knipping et al. (2015a, b) for the formation of Los Colorados. The predicted variations in $\delta^{56}Fe_{mgt}$ cover the ranges measured in the igneous and magmatic-hydrothermal magnetite from Los Colorados, respectively. We conclude that *in situ* Fe isotope analyses together with trace element composition of magnetite grains (1) can provide important insights about the source and evolution of magnetite-rich ore deposits, and (2) confirm the magnetite-flotation model as a plausible scenario for the formation of Kiruna-type IOA deposits.

Acknowledgments

We appreciate constructive comments of two anonymous reviewers. Jaayke Knipping thanks the German Academic Scholarship Foundation for a PhD scholarship. Adam Simon and Adrian Fiege acknowledge funding from the U.S. National Science Foundation (EAR 1250239 and 152439), and the University of Michigan. Martin Reich acknowledges funding provided by the Millennium Science Initiative (MSI) grant NC130065 "Millennium Nucleus for Metal Tracing along Subduction", and additional support by FONDAP project 15090013 ''Centro de Excelencia en Geotermia de los Andes, CEGA".

References

Arévalo, C., Grocott, J. and Welkner, D. (2003) The Atacama Fault System in the Huasco province, southern Atacama Desert, Chile. In Proceedings of the 10th Congreso Geológico Chileno, p 1-5.

Barton, M. D. and Johnson, D. A. (1996) Evaporitic-source model for igneous-related Fe oxide–(REE-Cu-Au-U) mineralization. Geology, 24(3), 259-262.

Barton, M. D. and Johnson, D. A. (2004) Footprints of Fe-oxide (-Cu-Au) systems. University of Western Australia Special Publication, 33, 112-116.

Barton, M.D. (2014) Iron oxide(–Cu–Au–REE–P–Ag–U–Co) systems. In H. Holland and K. Turekian, Eds., Treatise of Geochemistry, 16, p. 515-536.

Bell, A. and Simon, A.C. (2011) Evidence for the alteration of the $Fe^{3+}/\Sigma Fe$ of silicate melt caused by the degassing of chlorine-bearing aqueous volatiles. Geology. 39(5), 499-502.

Bigeleisen, J., & Mayer, M. G. (1947) Calculation of equilibrium constants for isotopic exchange reactions. The Journal of Chemical Physics, 15(5), 261-267.

Bilenker, L.D., Simon, A., Lundstrom, C.C. and Gajos, N. (2012) Iron isotope fractionation among magnetite, pyrrhotite, chalcopyrite, rhyolite melt and aqueous fluid at magmatic-hydrothermal conditions. AGU Fall Meeting, ID: V11A-2734, San Francisco, CA, USA.

Bilenker, L.D., Simon, A.C., Reich, M., Lundstrom, C.C., Gajos, N., Bindeman, I., Barra, F. and Munizaga, R. (2016) Fe–O stable isotope pairs elucidate a high-temperature origin of Chilean iron oxide-apatite deposits. Geochimica et Cosmochimica Acta, 177, 94-104.

Broman, C., Nyström, J. O., Henríquez, F. and Elfman, M. (1999) Fluid inclusions in magnetite-apatite ore from a cooling magmatic system at El Laco, Chile. GFF, 121(3), 253-267.

Burgisser, A. and Scaillet, B. (2007). Redox evolution of a degassing magma rising to the surface. Nature, 445(7124), 194.

CAPpresentationNEVASASeptember (2013) <http://www.cap.cl/wp/content/uploads/2013/09/cap_presentacion_nevasa_septiembre_2013.pdf>.

Carew, M. J. (2004) Controls on Cu-Au mineralisation and Fe oxide metasomatism in the Eastern Fold Belt, P.h.D thesis, James Cook University, NW Queensland, Australia.

Carmichael, D. M. (1969). On the mechanism of prograde metamorphic reactions in quartz-bearing pelitic rocks. Contributions to Mineralogy and Petrology, 20(3), 244-267.

589 Carmichael, I. S. (1991) The redox states of basic and silicic magmas: a reflection of their source
590 regions? Contributions to Mineralogy and Petrology, 106(2), 129-141.

591 Chen, H., Clark, A.H. and Kyser, T.K. (2010) The Marcona Magnetite Deposit, Ica, South-
592 Central Peru: A Product of Hydrous, Iron Oxide-Rich Melts? Economic Geologist, 105, 1441–
593 1456.

594 Dare, S. A., Barnes, S. J. and Beaudoin, G. (2012) Variation in trace element content of
595 magnetite crystallized from a fractionating sulfide liquid, Sudbury, Canada: Implications for
596 provenance discrimination. Geochimica et Cosmochimica Acta, 88, 27-50.

597 Dauphas, N. and Rouxel, O. (2006) Mass spectrometry and natural variations of iron isotopes.
598 Mass Spectrometry Reviews, 25(4), 515-550.

599 Dauphas, N., John, S. G. and Rouxel, O. (2017) Iron isotope systematics. Reviews in Mineralogy
600 and Geochemistry, 82(1), 415-510.

601 Dupuis, C. and Beaudoin, G. (2011) Discriminant diagrams for iron oxide trace element
602 fingerprinting of mineral deposit types. Mineralium Deposita 46, 319–335.

603 Edmonds, M., Brett, A., Herd, R.A., Humphreys, M.C.S. and Woods, A. (2015) Magnetite-
604 bubble aggregates at mixing interfaces in andesite magma bodies. Geological Society, London,
605 Special Publications, 410(1), 95-121

606 Ewart, A. and Griffin, W. L. (1994) Application of proton-microprobe data to trace-element
607 partitioning in volcanic rocks. Chemical Geology, 117(1-4), 251-284.

608 Ghiorso, M.S. and Sack, R.O. (1995) Chemical Mass Transfer in Magmatic Processes IV. A
609 revised and internally consistent thermodynamic model for the interpolation and extrapolation of
610 liquidsolid equilibria in magmatic systems at elevated temperatures and pressures. Contributions
611 to Mineralogy and Petrology 119, 197–212.

612 Ghiorso, M. S. and Evans, B. W. (2008). Thermodynamics of rhombohedral oxide solid
613 solutions and a revision of the Fe-Ti two-oxide geothermometer and oxygen-barometer.
614 American Journal of Science, 308(9), 957-1039.

615 Gardner, J. E. and Denis, M.-H. (2004) Heterogeneous bubble nucleation on Fe-Ti oxide crystals
616 in high-silica rhyolite melts. Geochimica et Cosmochimica Acta, 68, 3587-3597.

617 Gualda, G.A.R and Ghiorso, M.S. (2007) Magnetite scavenging and the buoyancy of bubbles in
618 magmas. Part 2: Energetics of crystal-bubble attachment in magmas. Contributions to
619 Mineralogy and Petrology, 154, 479–490.

620 Haynes, D. W., Cross, K. C., Bills, R. T. and Reed, M. H. (1995) Olympic Dam ore genesis; a
621 fluid-mixing model. Economic Geology, 90(2), 281-307.

Haynes, D.W. (2000) Iron oxide copper (-gold) deposits: their position in the ore deposit spectrum and modes of origin. In T.M. Porter, Ed., Hydrothermal Iron Oxide Copper-Gold and Related Deposits: A Global Perspective, p. 71-90. Australian Mineral Foundation, Adelaide.

Heimann, A., Beard, B. L. and Johnson, C. M. (2008) The role of volatile exsolution and sub-solidus fluid/rock interactions in producing high 56Fe/54Fe ratios in siliceous igneous rocks. Geochimica et Cosmochimica Acta, 72(17), 4379-4396.

Henríquez, F., Naslund, H. R., Nyström, J. O., Vivallo, W., Aguirre, R., Dobbs, F. M. and Lledó, H. (2003) New field evidence bearing on the origin of the El Laco magnetite deposit, northern Chile—a discussion. Economic Geology, 98(7), 1497-1500.

Hess, J. C., Lippolt, H. J., Gurbanov, A. G. and Michalski, I. (1993) The cooling history of the late Pliocene Eldzhurtinskiy granite (Caucasus, Russia) and the thermochronological potential of grain-size/age relationships. Earth and Planetary Science Letters, 117(3-4), 393-406.

Horn, I., von Blanckenburg, F., Schoenberg, R., Steinhoefel, G. and Markl, G. (2006) In situ iron isotope ratio determination using UV-femtosecond laser ablation with application to hydrothermal ore formation processes. Geochimica et Cosmochimica Acta, 70(14), 3677-3688.

Horn, I. and von Blanckenburg, F. (2007) Investigation on elemental and isotopic fractionation during 196 nm femtosecond laser ablation multiple collector inductively coupled plasma mass spectrometry. Spectrochimica Acta Part B: Atomic Spectroscopy, 62(4), 410-422.

Hou, T., Charlier, B., Namur, O., Schütte, P., Schwarz-Schampera, U., Zhang, Z. and Holtz, F. (2017) Experimental study of liquid immiscibility in the Kiruna-type Vergenoeg iron–fluorine deposit, South Africa. Geochimica et Cosmochimica Acta, 203, 303-322.

Hou, T., Charlier, B., Holtz, F., Veksler, I., Zhang, Z., Thomas, R. and Namur, O. (2018) Immiscible hydrous Fe–Ca–P melt and the origin of iron oxide-apatite ore deposits. Nature Communications, 9(1), 1415.

Hurwitz, S. and Navon, O. (1994) Bubble nucleation in rhyolitic melts: Experiments at high pressure, temperature, and water content. Earth and Planetary Science Letters, 122, 267-280
Grigsby, J. D. (1990). Detrital magnetite as a provenance indicator. Journal of Sedimentary Research, 60(6).

Knipping, J. L., Bilenker, L. D., Simon, A. C., Reich, M., Barra, F., Deditius, A. P., Lundstrom, C., Bindeman, I. and Munizaga, R. (2015a) Giant Kiruna-type deposits form by efficient flotation of magmatic magnetite suspensions. Geology, 43(7), 591-594.

Knipping, J. L., Bilenker, L. D., Simon, A. C., Reich, M., Barra, F., Deditius, A. P., Wälle, M., Heinrich, C.A., Holtz, F.and Munizaga, R. (2015b) Trace elements in magnetite from massive iron oxide-apatite deposits indicate a combined formation by igneous and magmatic-hydrothermal processes. Geochimica et Cosmochimica Acta, 171, 15-38.

Kreiner DC (2011) Epithermal Style Iron Oxide(–Cu–Au) (=IOCG) Vein Systems and Related Alteration, 659p. Ph.D. thesis, University of Arizona.

La Tourrette, T. Z., Burnett, D. S. and Bacon, C. R. (1991) Uranium and minor-element partitioning in Fe-Ti oxides and zircon from partially melted granodiorite, Crater Lake, Oregon. Geochimica et Cosmochimica Acta, 55(2), 457-469.

Lindsley, D.H. (1976) The crystal chemistry and structure of oxide minerals as exemplified by the Fe–Ti oxides. In D. Rumble III, Ed., Oxide Minerals, p. L1–L60. Reviews in Mineralogy and Geochemistry, Mineralogical Society of America.

Lindsley, D. H. (1991) Oxide minerals: petrologic and magnetic significance. Review in Mineralogy, 25, 509.

Martel, C., Pichavent, M., Holtz, F. and Scaillet, B. (1999) Effects of fO_2 and H_2O on andesite phase relations between 2 and 4 kbar. Journal of Geophysical Research 104, 29453-29470

Mathez, E. A. (1984) Influence of degassing on oxidation states of basaltic magmas. Nature, 310(5976), 371.

Menard, J. J. (1995) Relationship between altered pyroxene diorite and the magnetite mineralization in the Chilean Iron Belt, with emphasis on the El Algarrobo iron deposits (Atacama region, Chile). Mineralium Deposita, 30(3-4), 268-274.

Nadoll, P., Angerer, T., Mauk, J. L., French, D. and Walshe, J. (2014) The chemistry of hydrothermal magnetite: A review. Ore Geology Reviews, 61, 1-32.

Naslund, H. R. (2002) Magmatic iron ores and associated mineralization: examples from the Chilean High Andes and Coastal Cordillera. In T.M. Porter, Ed., Hydrothermal Iron Oxide Copper-Gold and Related Deposits: A Global Perspective 2, p. 207-226, PGC Publishing.

Nielsen, R. L. (1992) BIGD. FOR: a FORTRAN program to calculate trace-element partition coefficients for natural mafic and intermediate composition magmas. Computers & Geosciences, 18(7), 773-788.

Nielsen, R. L., Forsythe, L. M., Gallahan, W. E. and Fisk, M. R. (1994) Major-and trace-element magnetite-melt equilibria. Chemical Geology, 117(1-4), 167-191.

Nystroem, J. O. and Henriquez, F. (1994) Magmatic features of iron ores of the Kiruna type in Chile and Sweden; ore textures and magnetite geochemistry. Economic Geology, 89(4), 820-839.

Oeser, M., Weyer, S., Horn, I. and Schuth, S. (2014) High-Precision Fe and Mg Isotope Ratios of Silicate Reference Glasses Determined In Situ by Femtosecond LA-MC-ICP-MS and by Solution Nebulisation MC-ICP-MS. Geostandards and Geoanalytical Research, 38(3), 311-328.

693 Okamoto, K. (1979) Geochemical study on magmatic differentiation of Asama Volcano, central
694 Japan. The Journal of the Geological Society of Japan. 85, 525–535.
695
696 Pincheira, M., Thiele, R., and Fontbote, L. (1990) Tectonic Transpression along the Southern
697 Segment of the Atacam Fault-Zone, Chile. In Colloques et Seminaires: Symposium International
698 Geodynamique Andine, p. 133-136. Grenoble, France.

699 Poitrasson, F. and Freydier, R. (2005) Heavy iron isotope composition of granites determined by
700 high resolution MC-ICP-MS. Chemical Geology, 222(1-2), 132-147.

701 Pollard, P. J. (2006). An intrusion-related origin for Cu–Au mineralization in iron oxide–copper–
702 gold (IOCG) provinces. Mineralium Deposita, 41(2), 179.

703 Polyakov, V. B., Clayton, R. N., Horita, J. and Mineev, S. D. (2007) Equilibrium iron isotope
704 fractionation factors of minerals: reevaluation from the data of nuclear inelastic resonant X-ray
705 scattering and Mössbauer spectroscopy. Geochimica et Cosmochimica Acta, 71(15), 3833-3846.

706 Rhodes, A. L. and Oreskes, N. (1995) Magnetite deposition at El Laco, Chile: implications for
707 Fe-oxide formation in magmatic-hydrothermal systems. In A.H. Clark, Ed., Proceedings of the
708 second giant ore deposits workshop, p. 582-622.

709 Rhodes, A. L. and Oreskes, N. (1999) Oxygen isotope composition of magnetite deposits at El
710 Laco, Chile: Evidence of formation from isotopically heavy fluids. In B.J. Skinner, Ed., Geology
711 and Ore Deposits of the Central Andes, p. 333-351. Society of Economic Geologists Special
712 Publication, 7.

713 Rhodes A. L., Oreskes N. and Sheets S. (1999) Geology and rare earth element geochemistry of
714 magnetite deposits at El Laco, Chile. In B.J. Skinner, Ed., Geology and Ore Deposits of the
715 Central Andes, p. 299-332. Society of Economic Geologists Special Publication, 7.

716 Rojas, P. A., Barra, F., Reich, M., Deditius, A., Simon, A., Uribe, F., Romero, R. and Rojo, M.
717 (2018) A genetic link between magnetite mineralization and diorite intrusion at the El Romeral
718 iron oxide-apatite deposit, northern Chile. Mineralium Deposita, 1-20.

719 Schauble E. A. (2004) Applying stable isotope fractionation theory to new systems. In C. M.
720 Johnson, B. L. Beard and F. Albarede, Eds., Geochemistry of Non-Traditional Stable Isotopes, p.
721 65-111. Reviews in Mineralogy and Geochemistry, Mineralogical Society of America,
722 Washington, DC, USA.

723 Schauble, E. A., Méheut, M. and Hill, P. S. (2009) Combining metal stable isotope fractionation
724 theory with experiments. Elements, 5(6), 369-374.

725 Schoenberg, R., and von Blanckenburg, F. (2006) Modes of planetary-scale Fe isotope
726 fractionation. Earth and Planetary Science Letters, 252(3-4), 342-359

727 Schuessler, J. A., Schoenberg, R., and Sigmarsson, O. (2009) Iron and lithium isotope
728 systematics of the Hekla volcano, Iceland—evidence for Fe isotope fractionation during magma
729 differentiation. Chemical Geology, 258(1), 78-91.

730 Severmann, S. and Anbar, A. D. (2009) Reconstructing paleoredox conditions through a multitracer
731 approach: the key to the past is the present. Elements, 5(6), 359-364.

732 Sillitoe, R. H. and Burrows, D. R. (2002) New field evidence bearing on the origin of the El
733 Laco magnetite deposit, northern Chile. Economic Geology, 97(5), 1101-1109.

734 Simon, A.C., Pettke, T., Candela, P.A., Piccoli, P.M. and Heinrich, A.H. (2004) Magnetite
735 solubility and iron transport in magmatic-hydrothermal environments. Geochimica et
736 Cosmochimica Acta, 68, 4905–4914.

737 Sossi, P. A., Foden, J. D. and Halverson, G. P. (2012) Redox-controlled iron isotope
738 fractionation during magmatic differentiation: an example from the Red Hill intrusion, S.
739 Tasmania. Contributions to Mineralogy and Petrology, 164(5), 757-772.

740 Sossi, P. A. and O'Neill, H. S. C. (2017) The effect of bonding environment on iron isotope
741 fractionation between minerals at high temperature. Geochimica et Cosmochimica Acta, 196,
742 121-143.

743 Telus, M., Dauphas, N., Moynier, F., Tissot, F. L., Teng, F. Z., Nabelek, P. I., Craddock, P.R.
744 and Groat, L. A. (2012) Iron, zinc, magnesium and uranium isotopic fractionation during
745 continental crust differentiation: The tale from migmatites, granitoids, and pegmatites.
746 Geochimica et Cosmochimica Acta, 97, 247-265.

747 Teng, F. Z., Dauphas, N. and Helz, R. T. (2008) Iron isotope fractionation during magmatic
748 differentiation in Kilauea Iki lava lake. Science, 320(5883), 1620-1622.

749 Toplis, M. J. and Carroll, M. R. (1995) An experimental study of the influence of oxygen
750 fugacity on Fe-Ti oxide stability, phase relations, and mineral—melt equilibria in ferro-basaltic
751 systems. Journal of Petrology, 36(5), 1137-1170.

752 Travisany V., Henriquez F. and Nyström J. O. (1995) Magnetite lava flows in the Pleito-Melon
753 District of the Chilean iron belt. Economic Geologist, 90, 438–444.

754 Uyeda, S. and Kanamori, H. (1979) Back-arc opening and the mode of subduction. Journal of
755 Geophysical Ressearch, 84,1049-1061.

756 Van Baalen, M. R. (1993) Titanium mobility in metamorphic systems: a review. Chemical
757 Geology, 110(1-3), 233-249.

758 Velasco, F. and Tornos, F. (2009) Pegmatite-like magnetite–apatite deposits of northern Chile: A
759 place in the evolution of immiscible iron oxide melts? In T. Bleninsop and M. Gettings, Eds.,

760 Proceedings of the 10th Biennial SGA Meeting, p. 665–667. Society for Geology Applied to Ore
761 Deposits, Townsville, Australia.
762
763 Verlaguet, A., Brunet, F., Goffé, B. and Murphy, W. M. (2006) Experimental study and
764 modeling of fluid reaction paths in the quartz–kyanite±muscovite–water system at 0.7 GPa in the
765 350–550 C range: Implications for Al selective transfer during metamorphism. Geochimica et
766 Cosmochimica Acta, 70(7), 1772-1788.

767 Wechsler, B. A., Lindsley, D. H. and Prewitt, C. T. (1984) Crystal structure and cation
768 distribution in titanomagnetites ($Fe_{3-x}Ti_xO_4$). American Mineralogist, 69(7-8), 754-770.

769 Weis, F. (2013) Oxygen and iron isotope systematics of the Grängesberg mining district (GMD),
770 Central Sweden, 83 p. Ph.D thesis, Uppsala University, Sweden.

771 Weyer, S. and Schwieters, J. B. (2003) High precision Fe isotope measurements with high mass
772 resolution MC-ICPMS. International Journal of Mass Spectrometry, 226(3), 355-368.

773 Zajacz, Z., Halter, W. E., Pettke, T. and Guillong, M. (2008) Determination of fluid/melt
774 partition coefficients by LA-ICPMS analysis of co-existing fluid and silicate melt inclusions:
775 Controls on element partitioning. Geochimica et Cosmochimica Acta, 72(8), 2169-2197.

776 Zambardi, T., Lundstrom, C., Li, X. and McCurry, M. (2014) Fe and Si isotope variations at
777 Cedar Butte volcano; insight into magmatic differentiation. Earth and Planetary Science Letters
778 405, 169-179.

779 Zheng, X.-Y., Beard, B.L. and Johnson, C.M. (2018) Assessment of matrix effects associated
780 with Fe isotope analysis using 266 nm femtosecond and 193 nm nanosecond laser ablation multi-
781 collector inductively coupled plasma mass spectrometry. Journal of Analytical Atomic
782 Spectrometry 33, 68–83.
783

784

785 **Figure captions**

786 **Fig. 1:** Maps of Los Colorados. a) Location of the Los Colorados IOA deposit in Chile.
787 Geological map shows the close relationship between Los Colorados and different plutons
788 (modified after Arévalo et al. 2003) associated with the Los Colorados Fault, which is the central
789 branch of the Atacama Fault System at this latitude. b) Plan view of Los Colorados IOA deposit
790 and locations of drill cores (LC-04 and LC-05).
791

Fig. 2: Trace element data for magnetite grains from Los Colorados (Knipping et al. 2015b). The data indicate a transition from high concentrations of [Ti+V] vs. [Al+Mn] (open red circles) typical for a high temperature magmatic (igneous) origin, towards lower trace element concentrations (open blue circles) consistent with precipitation from a cooling (magmatic-) hydrothermal fluid. Many samples are characterized by a distinct, intra-grain core-to-rim trace element zoning (filled red and blue circles connected by tie lines).

Fig. 3: Illustration of the flotation model modified from Knipping et al. (2015a,b): **a)** igneous magnetite crystallization and initial fluid bubble nucleation; **b)** further decompression-induced degassing and buoyancy-driven bubble-magnetite pair ascent; **c)** Fe enrichment of the saline bubble-magnetite suspension during continued ascent; and, **d)** efficient segregation of the magnetite suspension by hydraulic fracturing and precipitation of dissolved Fe. **e)** Schematic sketch of massive magnetite from Los Colorados, including igneous magnetite "cores" (black) with magmatic-hydrothermal magnetite "rims" (dark grey) and/or within a magmatic-hydrothermal magnetite "matrix" (light grey). Areas **A**, **B** and **C** are examples for possible sampling regions for the analyses of this study: **(A)** sampling typical igneous magnetite core with magmatic-hydrothermal rim, **(B)** sampling pure magmatic-hydrothermal magnetite matrix, **(C)** sampling an agglomerate of pure igneous magnetite crystals.

Fig. 4: $\delta^{57}Fe$ plotted against $\delta^{56}Fe$. The measured $\delta^{56}Fe$ and $\delta^{57}Fe$ values plot on a near-ideal trend (gray line; m = 1.42, R^2 = 0.9) for mass dependent isotope fractionation (black line; m = 1.47) allowing the comparability of our results with published $\delta^{57}Fe$ values.

Fig. 5: Reflected light image of sample LC-05-82.6a and trace element transect. The green box highlights the previous measured trace element transect by LA-ICP-MS (Knipping et al. 2015b). Red and blue values represent $\delta^{56}Fe$ data (in ‰) of raster areas collected by *in-situ* Fe-isotope LA-MC-ICP-MS. LA-ICP-MS elemental profiles are shown for Fe (black), Al (dark red) and Ti (dark green) indicating a sudden decrease in trace elements towards the grain rim that is also visible in EPMA trace element map for Ti.

Fig. 6: δ^{56}Fe vs. depth of sampled magnetite grains. **(a)** Results of drill core LC-04 and **(b)** results of drill core LC-05. Grey bands represent the magmatic range defined by Heimann et al. (2008), which include both pure igneous and magmatic-hydrothermal magnetite. Red symbols indicate igneous magnetite and blue data represent magmatic-hydrothermal magnetite rims/matrix from Los Colorados.

Fig. 7: Compatible trace element concentrations in magnetite vs. δ^{56}Fe indicate the compositional evolution of igneous magnetite with ongoing fluid exsolution shown by red arrow. Here, only those δ^{56}Fe data are plotted where previous LA-ICP-MS trace element analyses were collected in direct proximity.

Fig. 8: δ^{56}Fe vs. Sn in Los Colorados magnetite. Tin is more compatible in magnetite at more oxidizing conditions (Carew, 2004) suggesting oxidation during decompression-induced crystallization (Mathez, 1984; Burgisser and Scaillet, 2007; Bell and Simon, 2011). Here, only those δ^{56}Fe data are plotted where previous LA-ICP-MS trace element analyses were collected in direct proximity.

Fig. 9: MELTS models using the P1D andesite composition (Martel et al. 1999), 1050 °C, NNO+3 and 6 wt% H_2O. **(a)** wt% of the existing phases (melt, mgt and fluid) and **(b)** Fe fraction between existing phases during decompression from 250 to 75 MPa. 35 wt% $NaCl_{eq}$ was assumed for the fluid (according to Knipping et al. 2015b) and thus a partition coefficient of $D^{f/m}_{Fe}$=8.5 (Zajacz et al., 2008) was used to calculate the Fe concentration in the fluid. *Initial igneous mgt* indicates the amount of mgt crystallized prior to decompression and *new igneous mgt* indicates the amount of mgt crystallized during/after decompression.

Fig. 10: Predicted Fe isotope evolution of co-existing melt, fluid and magnetite. The δ^{56}Fe values for melt and fluid represent the bulk remaining Fe isotope composition at a given fraction. In contrast, the δ^{56}Fe values displayed for magnetite represent the "snapshot" Fe isotope composition at a given *f*. This allows direct comparison of the δ^{56}Fe values for magnetite to the measured values, presuming grain-to-grain and within grain diffusive re-equilibration is negligible (unless for closed-system scenario). *Stage 1:* Cooling-induced crystallization of *initial*

igneous mgt in the magma reservoir. *Stage 2*: Decompression-induced degassing and crystallization of *new igneous mgt* in the magma reservoir. At the end of Stage 2 a fluid-magnetite suspension is separated from the magma reservoir. *Stage 3*: Cooling-induced precipitation of magmatic-hydrothermal magnetite from a separated fluid at shallow depth.

Assumed conditions contain an andesitic melt with a $\delta^{56}Fe_{bulk}$ = 0.11 ‰ (red star) at 250 MPa with 6 wt% dissolved H_2O. Decompression is assumed down to 75 MPa with the exsolution of ~2.8 wt% H_2O with a molality of 5.9 m Cl (= 35 wt% $NaCl_{eq}$). The red and blue areas highlight the average $\delta^{56}Fe$ (± 2σ) of the measured and assigned igneous (0.24 ± 0.07 ‰) and magmatic-hydrothermal magnetite grains (0.15 ± 0.05 ‰), respectively.

Comparison to Fig. 3: Fig. 3a represents end of Stage 1 and beginning of Stage 2; Fig. 3b-c represents Stage 2; Fig. 3d represents Stage 3.

This is a preprint, the final version is subject to change, of the American Mineralogist (MSA)
Cite as Authors (Year) Title. American Mineralogist, in press.
DOI: https://doi.org/10.2138/am-2019-6623

Table 1: δ^{56}Fe and trace element concentrations of Los Colorados magnetite. Trace element concentrations are only given for those in-situ δ^{56}Fe raster spots where trace element transects were measured by LA-ICP-MS in direct proximity. The magnetites were assigned as igneous (magm.) or magmatic-hydrothermal (hydro.), based on their Al and Ti concentrations and/or textural appearance.

		#	δ^{56}Fe [‰]	2 σ	Al [ppm]	Ti [ppm]	V [ppm]	Mn [ppm]	Zn [ppm]	Ga [ppm]	defined as
LC-05-20.7b		A	0.12	0.06	4458	2439	2965	1546	254	65	magm.
depth [m]	**20.7**	B	0.15	0.06	4458	2439	2965	1546	254	65	magm.
core/rim	**no**	C	0.08	0.05	4764	2617	3015	1830	304	68	magm.
		D	0.06	0.05	-	-	-	-	-	-	magm.
LC-05-82.6a		A	0.16	0.04	1315	568	3031	1297	173	59	hydro.
depth [m]	**82.6**	B	0.20	0.05	2476	2019	3057	1636	225	68	magm.
core/rim	**yes**	C	0.21	0.05	2476	2019	3057	1636	225	68	magm.
		D	0.24	0.05	-	-	-	-	-	-	magm.
		E	0.19	0.05	-	-	-	-	-	-	magm.
		F	0.21	0.05	-	-	-	-	-	-	magm.
LC-05-106d		A	0.23	0.05	2389	679	3132	1275	188	51	hydro.
depth [m]	**106**	B	0.25	0.05	3012	1274	3146	1732	229	57	magm.
core/rim	**yes**	C	0.25	0.05	-	-	-	-	-	-	magm.
		D	0.27	0.05	-	-	-	-	-	-	magm.
LC-06-126a		A	0.10	0.05	1898	644	2909	1110	149	65	hydro.
depth [m]	**126**	B	0.13	0.05	2005	660	2954	1093	124	63	hydro.
core/rim	**no**	C	0.10	0.05	-	-	-	-	-	-	hydro.
		D	0.09	0.05	-	-	-	-	-	-	hydro.
		E	0.12	0.05	-	-	-	-	-	-	hydro.
		F	0.12	0.05	-	-	-	-	-	-	hydro.
LC-05-150b		A	0.14	0.05	5123	7396	7089	1740	388	72	magm.
depth [m]	**150**	B	0.20	0.05	-	-	-	-	-	-	magm.
core/rim	**no**										
LC-04-38.8b		A	0.25	0.05	2444	1249	2556	517	74	62	magm.
depth [m]	**38.8**	B	0.16	0.06	667	916	2471	290	14	50	hydro.
core/rim	**yes**	C	0.26	0.05	2807	1508	2623	553	51	61	magm.
		D	0.27	0.05	2807	1508	2623	553	51	61	magm.
		E	0.31	0.05	-	-	-	-	-	-	magm.

		F	0.30	0.05	-	-	-	-	-	-	magm.
		G	0.27	0.05	-	-	-	-	-	-	magm.
		H	0.32	0.05	-	-	-	-	-	-	magm.
LC-04-38.8d		A	0.38	0.05	2283	1281	1988	652	75	60	magm.
depth [m]	**38.8**	B	0.36	0.05	3337	1385	2009	602	64	62	magm.
core/rim	**no**	C	0.32	0.05	-	-	-	-	-	-	magm.
		D	0.25	0.05	-	-	-	-	-	-	magm.
LC-04-66.7b		A	0.21	0.05	412	132	1105	671	47	43	hydro.
depth [m]	**66.7**	B	0.15	0.05	693	111	1085	828	106	54	hydro.
core/rim	**no**	E	0.15	0.05	693	111	1085	828	106	54	hydro.
		F	0.22	0.04	693	111	1085	828	106	54	hydro.
		G	0.21	0.04	-	-	-	-	-	-	hydro.
		H	0.21	0.05	-	-	-	-	-	-	hydro.
LC-04-104c		A	0.21	0.06	1745	2592	2643	746	157	59	hydro.
depth [m]	**104**	B	0.29	0.06	2773	6392	2684	1444	97	61	magm.
core/rim	**yes**	C	0.27	0.06	2773	6392	2684	1444	97	61	magm.
		D	0.25	0.06	2773	6392	2684	1444	97	61	magm.
		E	0.27	0.06	-	-	-	-	-	-	magm.
		F	0.13	0.07	-	-	-	-	-	-	hydro.
LC-04-125.3e		A	0.17	0.05	-	-	-	-	-	-	hydro.
depth [m]	**125.3**	B	0.15	0.05	2191	2607	2559	640	152	50	hydro.
core/rim	**no**	C	0.20	0.05	3307	3290	2527	1134	112	58	hydro.
		D	0.13	0.05	-	-	-	-	-	-	hydro.
		E	0.18	0.04	-	-	-	-	-	-	hydro.
LC-04-129.3c		A	0.11	0.04	1804	3799	3524	1177	88	60	hydro.
depth [m]	**129.3**	B	0.04	0.05	-	-	-	-	-	-	hydro.
core/rim	**no**										
LC-04-129.3d		A	0.21	0.05	4968	4768	3275	1461	143	69	magm.
depth [m]	**129.3**	B	0.18	0.05	5473	5420	3288	1519	161	68	magm.
core/rim	**no**	C	0.24	0.05	-	-	-	-	-	-	magm.
		D	0.21	0.05	-	-	-	-	-	-	magm.
LC-04-129.3e		A	0.16	0.05	-	-	-	-	-	-	hydro.
depth [m]	**129.3**	B	0.14	0.05	-	-	-	-	-	-	hydro.
core/rim	**no**										

867

868 **Table 2:** Compilation of literature data on $\delta^{56}Fe$ (measured or recalculated from $\delta^{57}Fe$) relative
869 to IRMM-14 for igneous silicate rocks with 55 wt% < SiO_2 < 70 wt%. The average of all studies
870 results in $\delta^{56}Fe = 0.11 \pm 0.04$ ‰.

Author	Average $\delta^{56}Fe$	Stdev, 2 sigma	n
Poitrasson and Freydier, 2005	0.11	0.01	3
Schoenberg and von Blanckenburg, 2006	0.12	0.01	10
Heimann et al. 2008	0.10	0.04	18
Teng et al. 2008	0.20	0.02	2
Schuessler et al. 2009	0.07	0.03	10
Sossi et al. 2012	0.14	0.05	8
Telus et al. 2012 (and references therein)	0.12	0.04	18
Zambardi et al. 2014	0.11	0.03	5
Average	**0.11**	**0.04**	**69**

871

872

873

874

875

876

877

This is a preprint, the final version is subject to change, of the American Mineralogist (MSA)
Cite as Authors (Year) Title. American Mineralogist, in press.
DOI: https://doi.org/10.2138/am-2019-6623

878 **Figure 1**

879 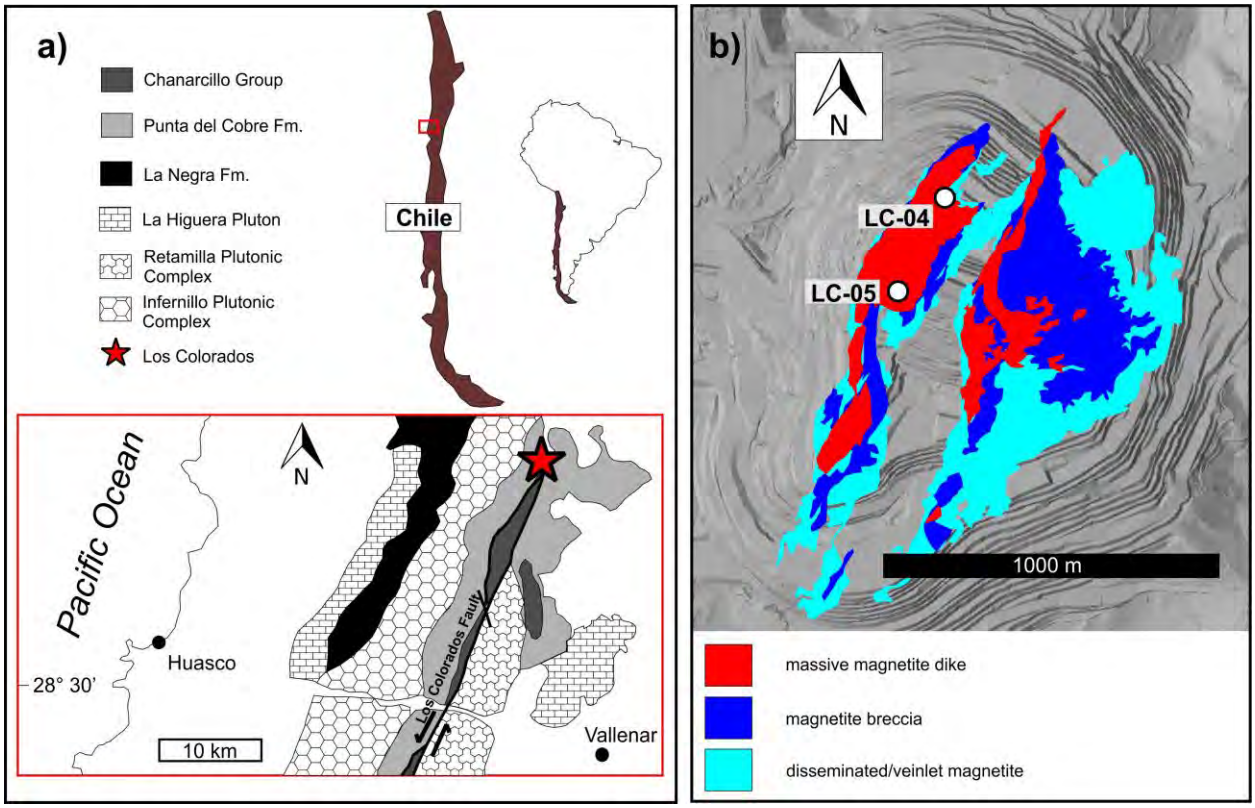

880

881

882

883

884

885

886

887

This is a preprint, the final version is subject to change, of the American Mineralogist (MSA)
Cite as Authors (Year) Title. American Mineralogist, in press.
DOI: https://doi.org/10.2138/am-2019-6623

888 **Figure 2**

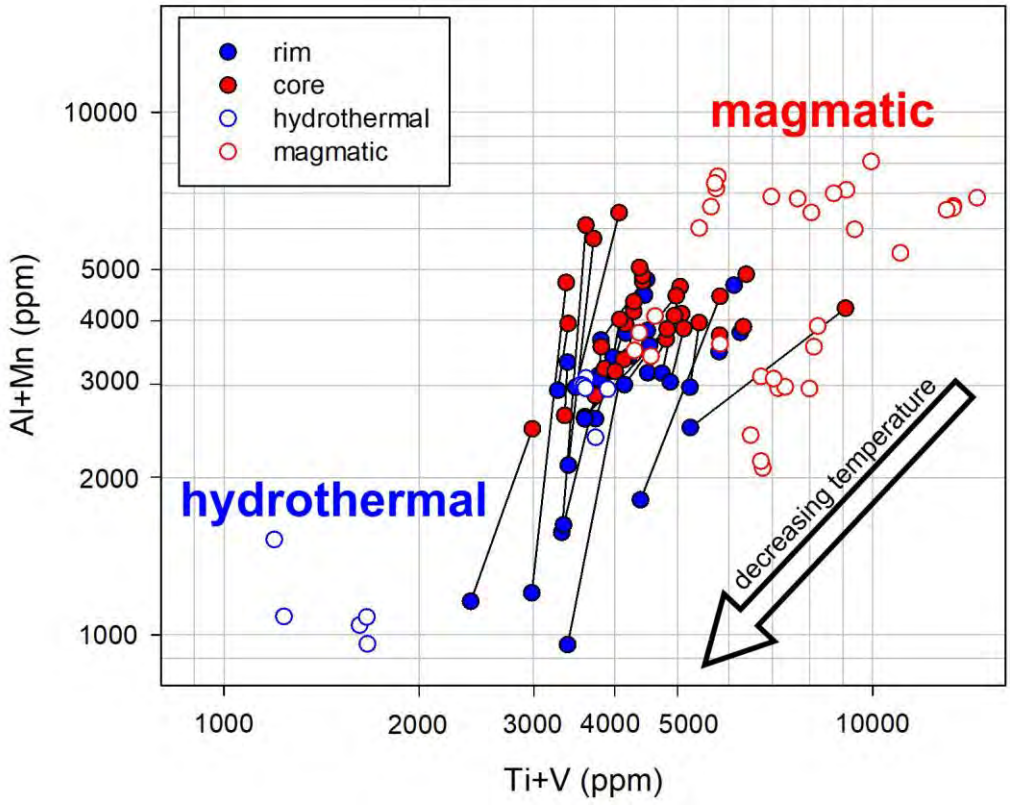

889

890

891

892

893

894

895

896

This is a preprint, the final version is subject to change, of the American Mineralogist (MSA)
Cite as Authors (Year) Title. American Mineralogist, in press.
DOI: https://doi.org/10.2138/am-2019-6623

897 **Figure 3**

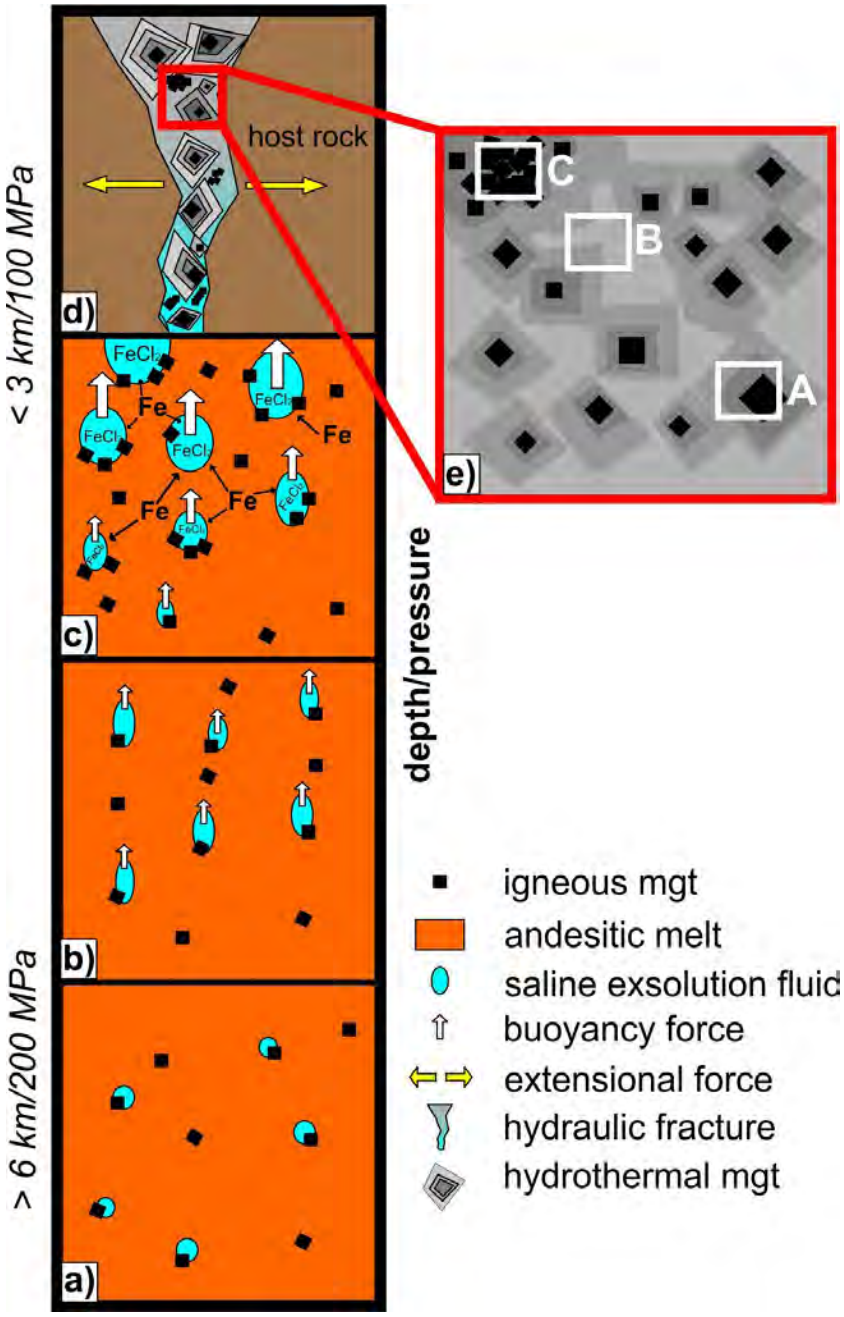

898

899

900

901 **Figure 4**

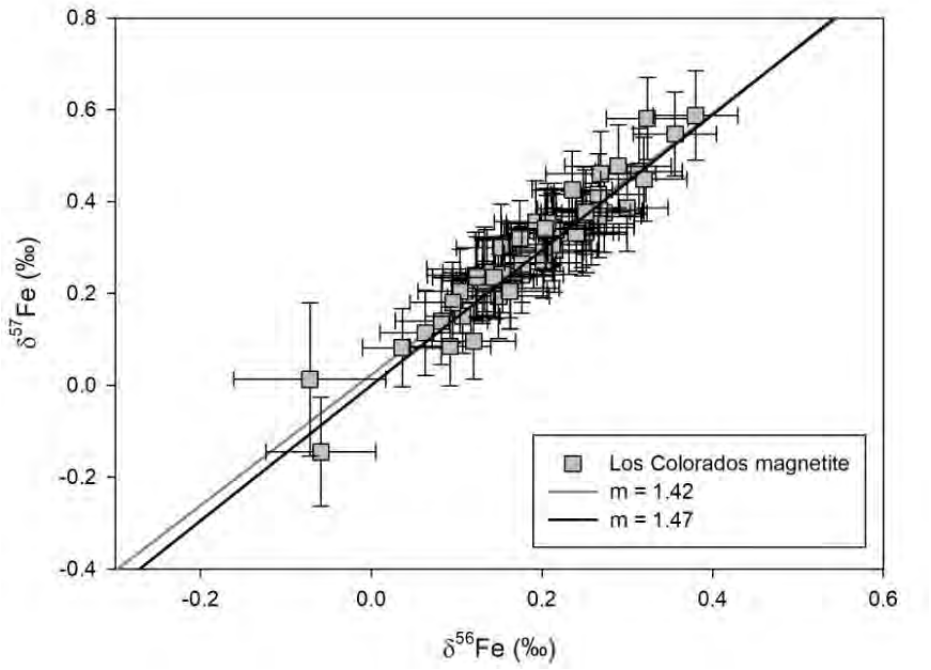

902

903

904

905

906

907

908

909

910

This is a preprint, the final version is subject to change, of the American Mineralogist (MSA)
Cite as Authors (Year) Title. American Mineralogist, in press.
DOI: https://doi.org/10.2138/am-2019-6623

911 **Figure 5**

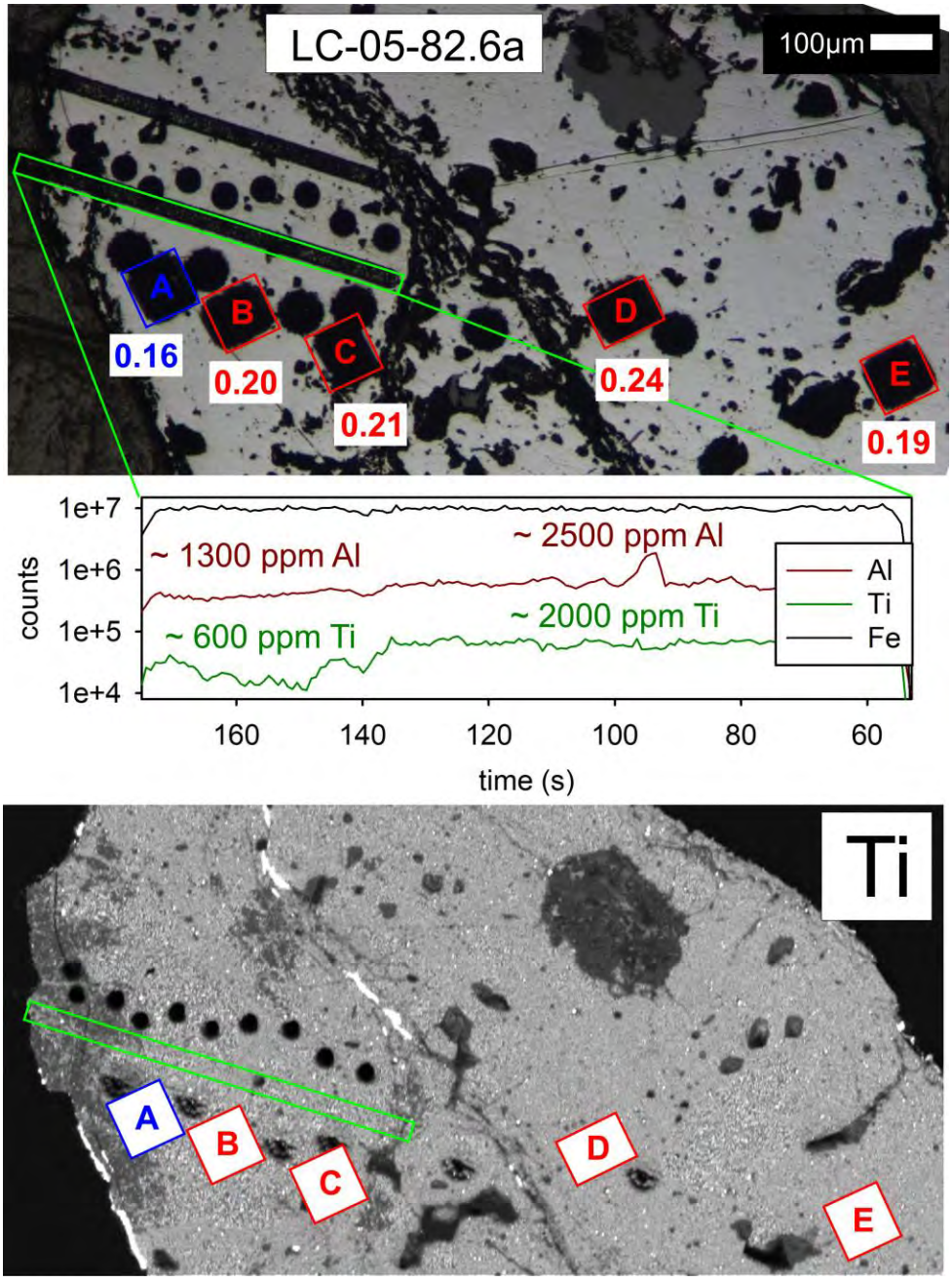

912

913

914

915 **Figure 6**

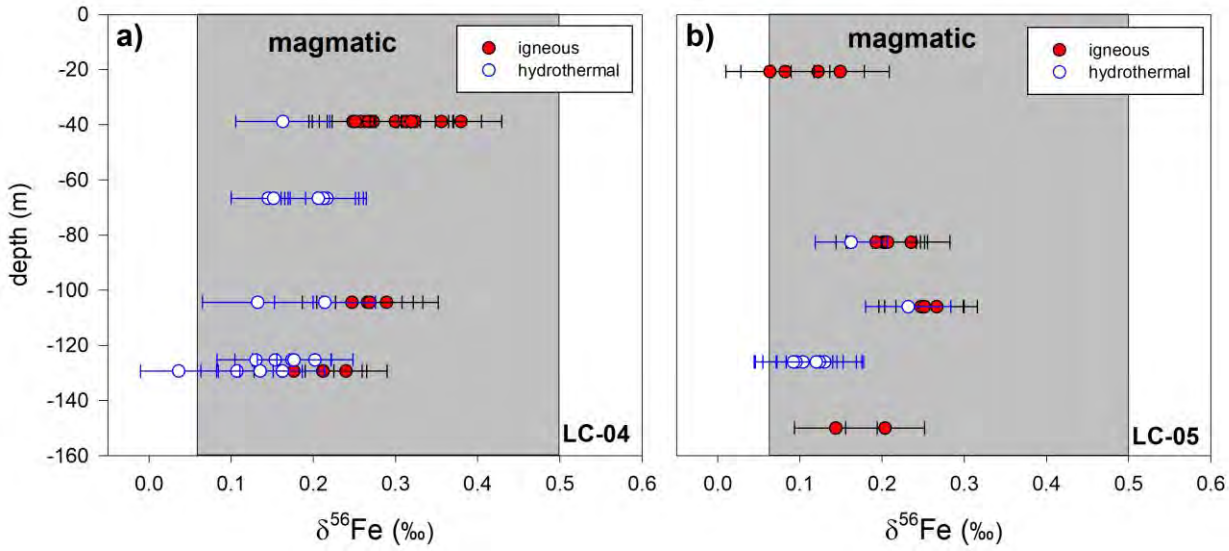

916

917

918

919

920

921

922

923

924

925

926

927 **Figure 7**

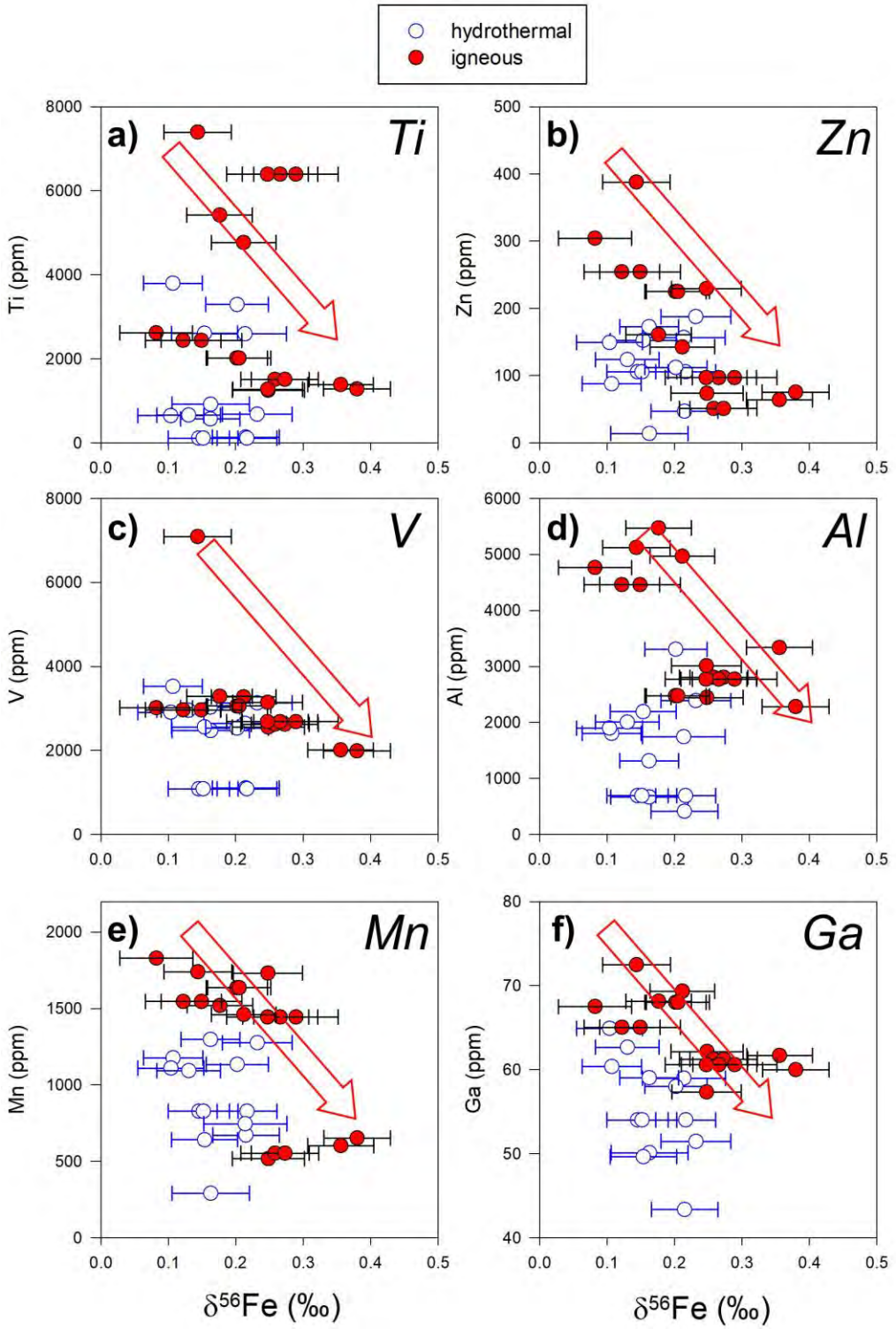

928

929 **Figure 8**

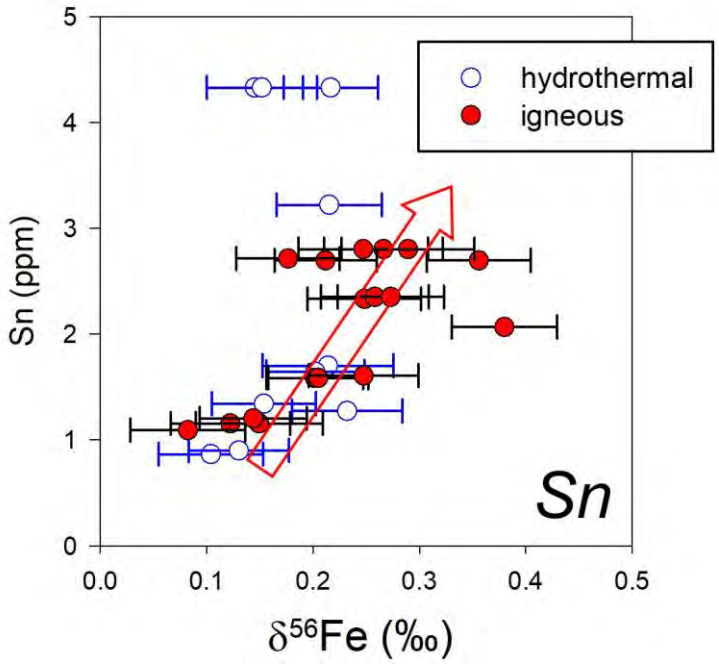

930

931

932

933

934

935

936

937

938

939

940 **Figure 9**

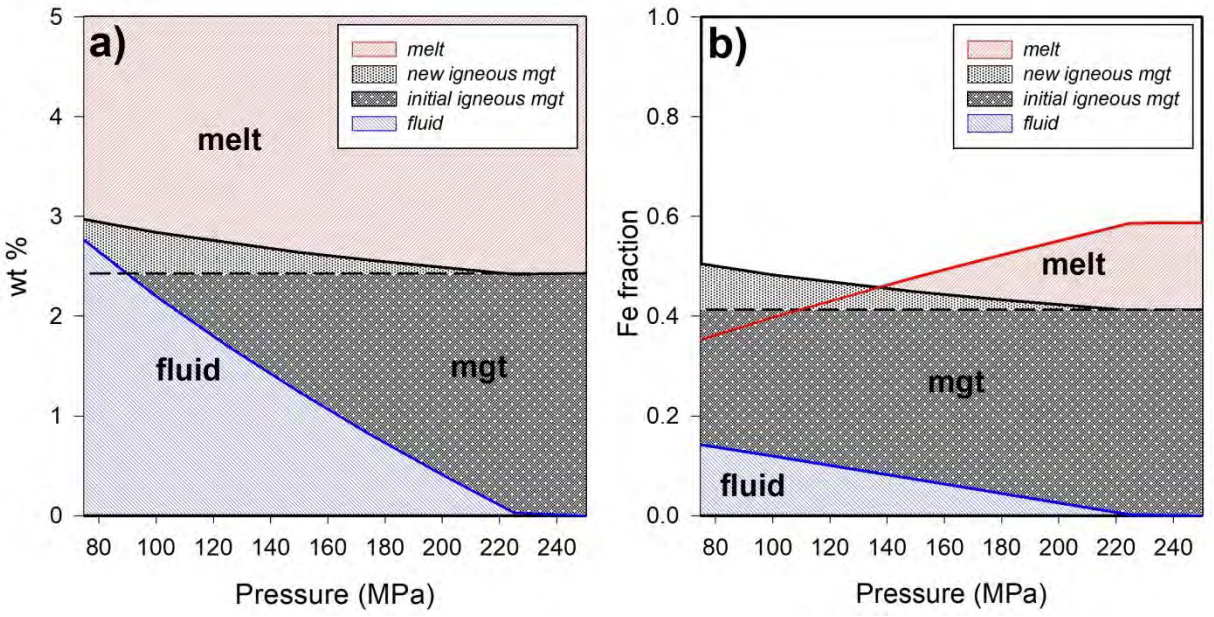

941

942

943

944

945

946

947

948

949

950

This is a preprint, the final version is subject to change, of the American Mineralogist (MSA)
Cite as Authors (Year) Title. American Mineralogist, in press.
DOI: https://doi.org/10.2138/am-2019-6623

951 **Figure 10**

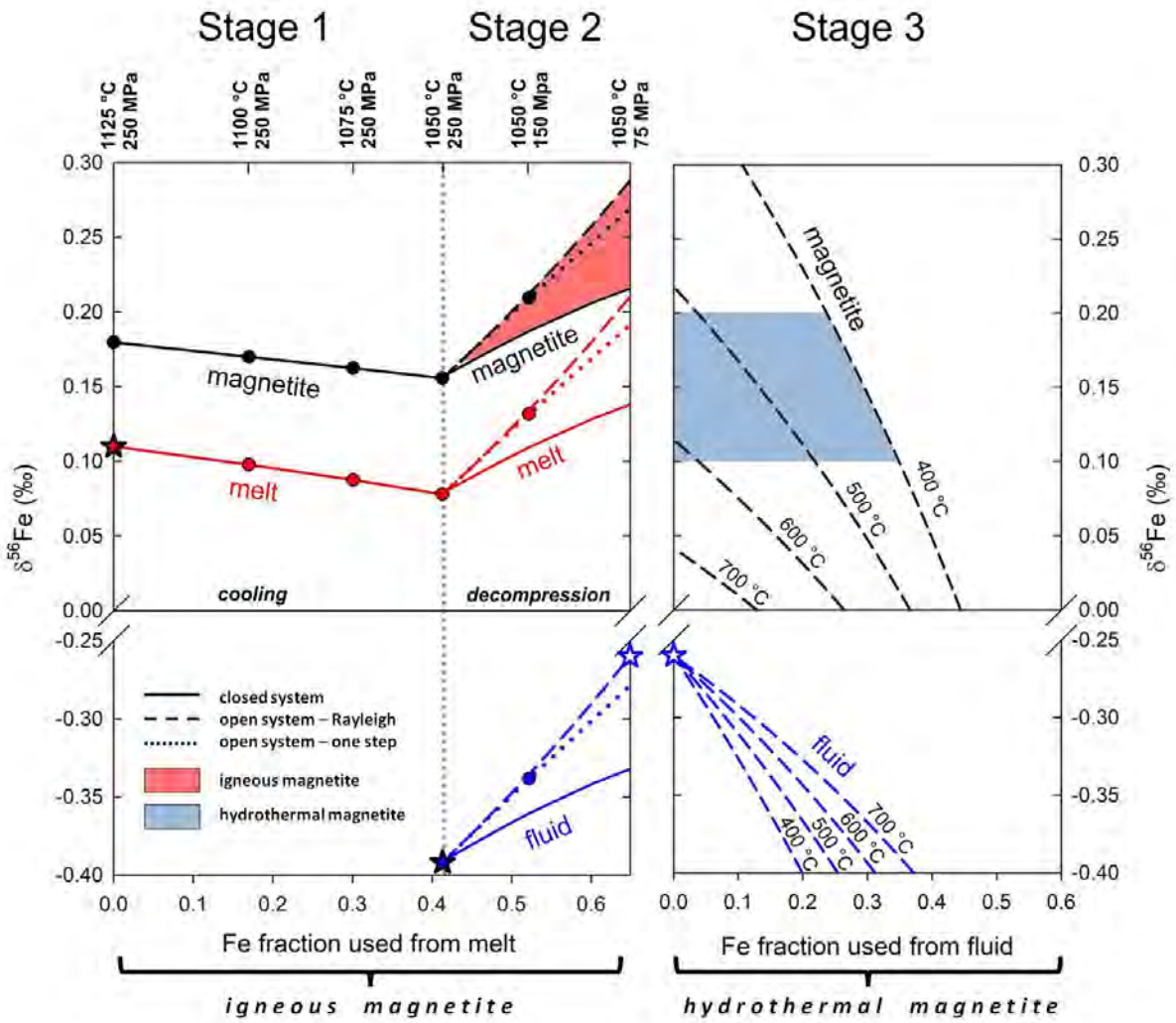

952

		#	δ^{56}Fe [‰]	2 σ	Al [ppm]	Ti [ppm]	V [ppm]
Sample ID	**LC-05-20.7b**	A	0.12	0.06	4458	2439	2965
depth [m]	**-20.7**	B	0.15	0.06	4458	2439	2965
core/rim	**no**	C	0.08	0.05	4764	2617	3015
		D	0.06	0.05	-	-	-
Sample ID	**LC-05-82-6a**	A	0.16	0.04	1315	568	3031
depth [m]	**-82.6**	B	0.20	0.05	2476	2019	3057
core/rim	**yes**	C	0.21	0.05	2476	2019	3057
		D	0.24	0.05	-	-	-
		E	0.19	0.05	-	-	-
		F	0.21	0.05	-	-	-
Sample ID	**LC-05-106d**	A	0.23	0.05	2389	679	3132
depth [m]	**-106**	B	0.25	0.05	3012	1274	3146
core/rim	**yes**	C	0.25	0.05	-	-	-
		D	0.27	0.05	-	-	-
Sample ID	**LC-05-126a**	A	0.10	0.05	1898	644	2909
depth [m]	**-126**	B	0.13	0.05	2005	660	2954
core/rim	**no**	C	0.10	0.05	-	-	-
		D	0.09	0.05	-	-	-
		E	0.12	0.05	-	-	-
		F	0.12	0.05	-	-	-
Sample ID	**LC-05-150b**	A	0.14	0.05	5123	7396	7089
depth [m]	**-150**	B	0.20	0.05	-	-	-
core/rim	**no**						
Sample ID	**LC-04-38.8b**	A	0.25	0.05	2444	1249	2556
depth [m]	**-38.8**	B	0.16	0.06	667	916	2471
core/rim	**yes**	C	0.26	0.05	2807	1508	2623
		D	0.27	0.05	2807	1508	2623
		E	0.31	0.05	-	-	-
		F	0.30	0.05	-	-	-
		G	0.27	0.05	-	-	-
		H	0.32	0.05	-	-	-
Sample ID	**LC-04-38.8d**	A	0.38	0.05	**2283**	**1281**	**1988**
depth [m]	**-38.8**	B	0.36	0.05	**3337**	**1385**	**2009**
core/rim	**no**	C	0.32	0.05	-	-	-
		D	0.25	0.05	-	-	-
Sample ID	**LC-04-66.7b**	A	0.21	0.05	412	132	1105
depth [m]	**-66.7**	B	0.15	0.05	693	111	1085
core/rim	**no**	E	0.15	0.05	693	111	1085
		F	0.22	0.04	693	111	1085

This is a preprint, the final version is subject to change, of the American Mineralogist (MSA)
Cite as Authors (Year) Title. American Mineralogist, in press.
DOI: https://doi.org/10.2138/am-2019-6623

		G	0.21	0.04	-	-	-
		H	0.21	0.05	-	-	-
Sample ID	**LC-04-104.4c**	A	0.21	0.06	1745	2592	2643
depth [m]	**-104**	B	0.29	0.06	2773	6392	2684
core/rim	**yes**	C	0.27	0.06	2773	6392	2684
		D	0.25	0.06	2773	6392	2684
		E	0.27	0.06	-	-	-
		F	0.13	0.07	-	-	-
Sample ID	**LC-04-125-3e**	A	0.17	0.05	-	-	-
depth [m]	**-125.3**	B	0.15	0.05	2191	2607	2559
core/rim	**no**	C	0.20	0.05	3307	3290	2527
		D	0.13	0.05	-	-	-
		E	0.18	0.04	-	-	-
Sample ID	**LC-04-129-3c**	A	0.11	0.04	1804	3799	3524
depth [m]	**-129.3**	B	0.04	0.05	-	-	-
core/rim	**no**						
Sample ID	**LC-04-129-3d**	A	0.21	0.05	4968	4768	3275
depth [m]	**-129.3**	B	0.18	0.05	5473	5420	3288
core/rim	**no**	C	0.24	0.05	-	-	-
		D	0.21	0.05	-	-	-
Sample ID	**LC-04-129.3e**	A	0.16	0.05	-	-	-
depth [m]	**-129.3**	B	0.14	0.05	-	-	-
core/rim	**no**						

This is a preprint, the final version is subject to change, of the American Mineralogist (MSA)
Cite as Authors (Year) Title. American Mineralogist, in press.
DOI: https://doi.org/10.2138/am-2019-6623

Mn [ppm]	Zn [ppm]	Ga [ppm]	defined as
1546	254	65	magm.
1546	254	65	magm.
1830	304	68	magm.
-	-	-	magm.
1297	173	59	hydro.
1636	225	68	magm.
1636	225	68	magm.
-	-	-	magm.
-	-	-	magm.
-	-	-	magm.
1275	188	51	hydro.
1732	229	57	magm.
-	-	-	magm.
-	-	-	magm.
1110	149	65	hydro.
1093	124	63	hydro.
-	-	-	hydro.
-	-	-	hydro.
-	-	-	hydro.
-	-	-	hydro.
1740	388	72	magm.
-	-	-	magm.
517	74	62	magm.
290	14	50	hydro.
553	51	61	magm.
553	51	61	magm.
-	-	-	magm.
-	-	-	magm.
-	-	-	magm.
-	-	-	magm.
652	**75**	**60**	magm.
602	**64**	**62**	magm.
-	-	-	magm.
-	-	-	magm.
671	47	43	hydro.
828	106	54	hydro.
828	106	54	hydro.
828	106	54	hydro.

-	-	-	hydro.
-	-	-	hydro.
746	157	59	hydro.
1444	97	61	magm.
1444	97	61	magm.
1444	97	61	magm.
-	-	-	magm.
-	-	-	hydro.
-	-	-	hydro.
640	152	50	hydro.
1134	112	58	hydro.
-	-	-	hydro.
-	-	-	hydro.
1177	88	60	hydro.
-	-	-	hydro.
1461	143	69	magm.
1519	161	68	magm.
-	-	-	magm.
-	-	-	magm.
-	-	-	hydro.
-	-	-	hydro.

author	average $\delta^{56}Fe$	2 sigma	n
Poitrasson and Freydier, 2005	0.11	0.01	3
Schoenberg and von Blanckenburg, 2006	0.12	0.01	10
Heimann et al. 2008	0.10	0.04	18
Teng et al. 2008	0.20	0.02	2
Schuessler et al. 2009	0.07	0.03	10
Sossi et al. 2012	0.14	0.05	8
Telus et al. 2012 (and references therein)	0.12	0.04	18
Zambardi et al. 2014	0.11	0.03	5
average	**0.11**	**0.04**	**69**